

The choice of embedding media affects image quality, tissue R2*, and susceptibility behaviors in post-mortem brain MR microscopy at 7.0 T

Petr Dusek^{1,2*}, Vince Istvan Madai³, Till Huelnhagen⁴, Erik Bahn⁵, Radoslav Matej^{6,7}, Jan Sobesky^{3,8}, Thoralf Niendorf^{4,8}, Julio Acosta-Cabronero^{9,10†}, and Jens Wuerfel^{11,12,13†}

¹ Department of Neurology, ² Department of Radiology, Charles University, 1st Faculty of Medicine and General University Hospital in Prague, Praha, Czech Republic;

³ Department of Neurology and Center for Stroke Research Berlin (CSB), Charité-Universitaetsmedizin, Berlin, Germany;

⁴ Berlin Ultrahigh Field Facility (B.U.F.F.), Max Delbrück Center for Molecular Medicine in the Helmholtz Association (MDC), Berlin, Germany;

⁵ Institute of Neuropathology, University Medicine Göttingen, Göttingen, Germany;

⁶ Department of Pathology and Molecular Medicine, Thomayer Hospital, Praha, Czech Republic;

⁷ Department of Pathology, Charles University, 1st Faculty of Medicine and General University Hospital in Prague, Praha, Czech Republic

⁸ Experimental and Clinical Research Center (ECRC), Charité-Universitaetsmedizin and Max Delbrück Center for Molecular Medicine in the Helmholtz Association (MDC), Berlin, Germany;

⁹ Wellcome Centre for Human Neuroimaging, UCL Institute of Neurology, University College London, London, United Kingdom;

¹⁰ German Center for Neurodegenerative Diseases (DZNE), Magdeburg, Germany;

¹¹ NeuroCure Clinical Research Center, Charité-Universitaetsmedizin, Berlin, Germany;

¹² Medical Imaging Analysis Center AG, Basel, Switzerland;

¹³ Dep. Biomedical Engineering, University Basel, Switzerland;

† J.A.-C. and J.W. share co-senior authorship

*Corresponding author:

Petr Dusek

Department of Neurology, 1st Faculty of Medicine and General University Hospital in Prague

Katerinska 30, 120 00, Praha 2, Czech Republic

E-mail: pdusek@gmail.com

Phone: (+420) 224 965 528

Running head: Postmortem MRI embedding

Word count: 5068

Abstract

Purpose: The quality and precision of post-mortem MRI microscopy may vary depending on the embedding medium employed. To investigate this, our study evaluated the impact of five widely used media on: (i) image quality, (ii) contrast of high spatial resolution gradient-echo (T_1 and T_2^* -weighted) MR images, (iii) effective transverse relaxation rate (R_2^*), and (iv) quantitative susceptibility measurements (QSM) of post-mortem brain specimens.

Methods: Five formaldehyde-fixed brain slices were scanned using 7.0 T MRI in: (i) formaldehyde solution (formalin), (ii) phosphate-buffered saline (PBS), (iii) deuterium oxide (D_2O), (iv) perfluoropolyether (Galden), and (v) agarose gel. Signal- and contrast-to-noise ratios (SNR/CNR) were calculated for cortex/white matter (WM) and basal ganglia/WM regions. In addition, median R_2^* and QSM values were extracted from caudate nucleus, putamen, globus pallidus, WM, and cortical regions.

Results: PBS, Galden, and agarose returned higher SNR/CNR compared to formalin and D_2O . Formalin fixation, and its use as embedding medium for scanning, increased tissue R_2^* . Imaging with agarose, D_2O and Galden returned lower R_2^* values than PBS (and formalin). No major QSM offsets were observed, though spatial variance was increased (with respect to R_2^* behaviors) for formalin and agarose.

Conclusions: Embedding media affect gradient-echo image quality, R_2^* and QSM in differing ways. In this study, PBS embedding was identified as the most stable experimental setup, although by a small margin. Agarose and Galden were preferred to formalin or D_2O embedding. Formalin significantly increased R_2^* causing noisier data and increased QSM variance.

Keywords

post-mortem imaging, ex vivo imaging, ultra-high field MRI, quantitative susceptibility mapping, formaldehyde fixation

Introduction:

MRI of *post-mortem* brain tissue is a widely used technique in neuroscience and in routine neuropathological examinations (1-3) to identify the extent and quantify the severity of structural alterations (4). High fidelity *post-mortem* MRI enables the detection and assessment of small lesions that are hardly visible on gross neuropathological examination (5). It is also used for validating quantitative MRI measurements (6-8) and for the systematic study of MRI contrast mechanisms in specific structures (9). An advantage of *post-mortem* imaging is that very long scanning sessions are feasible, enabling examinations with both, in-plane spatial resolution below 100 μm and high signal-to-noise ratio (SNR). This is often referred to as MR microscopy, which offers a high resolution view of tissue status often complementary to histochemical staining (10,11).

It is well established that SNR characteristics and sensitivity to magnetic susceptibility differences between substances are enhanced when imaging at ultra-high magnetic fields (UHF, $B_0 \geq 7.0$ T). Capitalizing on this, several UHF studies demonstrated the value of T_2^* and susceptibility-weighted MR microscopy to detect small numbers of iron-loaded dystrophic microglia or macrophages (12,13). However, many factors including natural tissue decomposition and chemical fixation may alter the MRI properties of *post-mortem* tissue (14,15) causing undesirable biases in the measurement. It is known that aldehyde fixation leads to gradual shortening of $T_1/T_2/T_2^*$ relaxation times, increased myelin water fraction, and apparent diffusivity reductions (1,16-22). The most rapid change in proton MR signal relaxation occurs during the first three weeks after fixation, which gradually plateaus prior to complete tissue penetration by the fixative agent, approximately three months after fixation (23-26). The impact of formaldehyde fixation on T_2 can be partially reversed by thorough washing with phosphate-buffered saline (14). Based upon these literature reports it is conceivable that quantitative MRI measures might differ across embedding media. In fact, a pilot study investigating this

phenomenon with fixed rat heart tissue found substantial differences (27). Although these results cannot be readily extrapolated to *post-mortem* imaging of human brain specimens, they highlight the importance of studying the impact of embedding media on MRI measurements.

The most widely used embedding media for imaging human tissue are formaldehyde solutions (28,29), phosphate-buffered saline (PBS) (30) and aqueous gels such as low-melting-point agarose (11,31). More recently, proton-free agents such as perfluoropolyether compounds (Fomblin® or Galden®, Solvay, Bruxelles, Belgium; Fluorinert™ FC-3283, 3M, Delft, Netherlands)(19,32-35), a wax-like compound (Paraplast®, Sigma-Aldrich, St.Louis, MI, USA)(36) or deuterium oxide (D₂O), are gaining popularity due to their ability to render dark background on MRI and their overall versatility. D₂O embedding, for example, has successfully been employed to suppress water signal for isolating myelin-protons (37,38). To date, however, no systematic methodological studies have investigated the differential impact of such media on fixed human tissue properties for MR microscopy. Motivated by this knowledge gap, in this study we aimed to evaluate the impact of five different types of embedding media on signal-to-noise ratio (SNR) and image contrast properties for high resolution anatomical imaging, effective transverse relaxation rate ($R_2^* = 1/T_2^*$) and bulk susceptibility MRI measurements from formaldehyde-fixed brain tissue specimens scanned in typical conditions of neuropathological examination.

Methods:

Brain specimens

We investigated post-mortem brain specimens from five subjects without known neurological history or conspicuous neuropathological finding. At the outset, whole brains were immersed in 4% (w/v) neutral-buffered formaldehyde solution (formalin). Then after one month, coronal slices (approximately 10 mm thick) were cut and re-immersed in formalin solution. For these experiments, representative slices containing the basal ganglia were chosen. Demographic information, post-mortem interval, and total fixation times are presented in Table 1.

Code	Source	Sex	Age at death	Medical history/cause of death	Postmortem interval (hours)	Fixation duration (months)	Embedding media order
PM-12	Gö	M	65	No medical history/ acute ileus with peritonitis	72	4	F-P-A-G-D
PM-13	Prg	M	61	Alcoholism, liver cirrhosis/ sepsis	10	2	F-P-G-A-D
PM-14	Prg	M	50	Diabetes mellitus, alcoholism, liver cirrhosis/ sepsis	26	2	F-P-G-A-D
PM-15	Gö	M	62	Spontaneous aortic rupture	18	3.5	F-P-D-A-G
PM-16	Gö	F	66	Acute cardiac failure due to cardiac infarction	80	3	F-P-D-G-A

Abbreviations: F=formalin; P=PBS; G=galden; D=D₂O; A=agarose; Gö=Institute of Neuropathology, University Medicine Göttingen; Prg= Department of Pathology and Molecular Medicine, Thomayer Hospital in Prague.

Experimental design

Brain slices were scanned in a custom-tailored container (MRI.TOOLS GmbH, Berlin, Germany) mounted between two polyacrylamide plates (Figure 1 A,B) using a 7T whole-body MRI system (Siemens Magnetom, Siemens Healthcare, Erlangen, Germany). A transmit-receive coil consisting of a birdcage volume coil for signal transmission coupled with a 24-channel head-array coil for reception (Nova Medical, Wilmington, MA, USA) was utilized.

Five consecutive imaging sessions were performed with brain slices immersed in different embedding media: (i) formalin (one batch of self-prepared, neutral-buffered [i.e. containing disodium hydrogen phosphate - dihydrate and dipotassium hydrogen phosphate] 4% formaldehyde solution), (ii) self-prepared PBS, (iii) D₂O (Sigma-Aldrich, St.Louis, MI, USA), (iv) Galden, and (v) 1.5% (w/v) agarose gel (UltraPure low melting point agarose, Life Technologies Corporation, Carlsbad, CA, USA) prepared in PBS solution.

All samples were first scanned in formalin. This was then followed by thorough PBS washing and subsequent scanning in PBS. After removing from formalin, samples were rinsed and were then kept for at least 3 hours in PBS during which several exchanges of fresh media were performed. To minimize potential bias due to persisting residual effect of previous embedding, the remaining media were used in a pseudorandom order for each specimen (Table 1). Between scanning sessions, slices were thoroughly washed with PBS for at least one hour and were then kept in the corresponding medium for at least one hour. For D₂O embedding, the fresh medium was exchanged once to facilitate tissue penetration and minimize PBS contributions. Of note, brain slices and embedding media were kept at room temperature in total for 2-5 hours to ensure stable thermal conditions during scanning (39). During scanning, embedding media temperatures were continuously monitored using a fiber optic temperature sensor (Neoptix Inc., Québec, Canada).

After immersing brain slices in each embedding medium, they were serially scanned using a 2D multi-echo, gradient-recalled echo (GRE) sequence (single slice, repetition time (TR) = 500 ms; echo time (TE) = 4.6, 10.7, 16.8, 22.9, 29.0, 35.0, 41.1, 47.2 ms; flip angle (FA) = 35°; voxel resolution = 0.47x0.47x2.0 mm³, 32 averages, scan time = 43:21 min), from which quantitative T₂* (effective transverse relaxation time) maps were inferred using scanner software. This was repeated to confirm samples were in a relatively stable (i.e. suitable) regime for scanning (Supporting Information Figure S1). Mean T₂* relaxation times were calculated from cortex, white matter (WM), and lentiform nucleus (LN) in predefined regions of interest (ROIs): three cortical ROIs in GRE isointense regions of insula, cingulate gyrus and lateral aspect of the hemisphere; three WM ROIs (also isointense on GRE images) adjacent to lateral ventricles and in temporal lobe; and two LN ROIs including whole putamen and globus pallidus (Figure 1C).

Subsequently, a protocol consisting of high-resolution 3D MPRAGE (TR = 2300 ms; TE = 5.9 ms; inversion time (TI) = 1000ms; FA=15°; voxel resolution = 0.14x0.14x0.5 mm³; 44 slices; total 15 averages [3 measurements with 5 averages]; scan time, 2 h 37 min) and dual-echo 3D GRE imaging (TR=31 ms; TE=6.1 and 19.4ms; FA=15°; voxel resolution = 0.14x0.14x0.5 mm³; 44 slices; total 15 averages [3 measurements with 5 averages]; scan time = 2 h 59 min) was applied. This high in-plane spatial resolution protocol, optimised for anatomical imaging, was used for qualitative assessment, SNR, and contrast-to-noise ratio (CNR) comparisons. In addition, R₂* relaxation rate and quantitative susceptibility mapping (QSM) were inferred from a multi-echo 3D GRE pulse sequence (TR=53 ms; TE=6.2, 17.3, 28.5, 39.8 ms; FA=24°; voxel resolution = 0.36x0.36x0.36 mm³; 44 slices; 10 averages; scan time, 3 h 24 min).

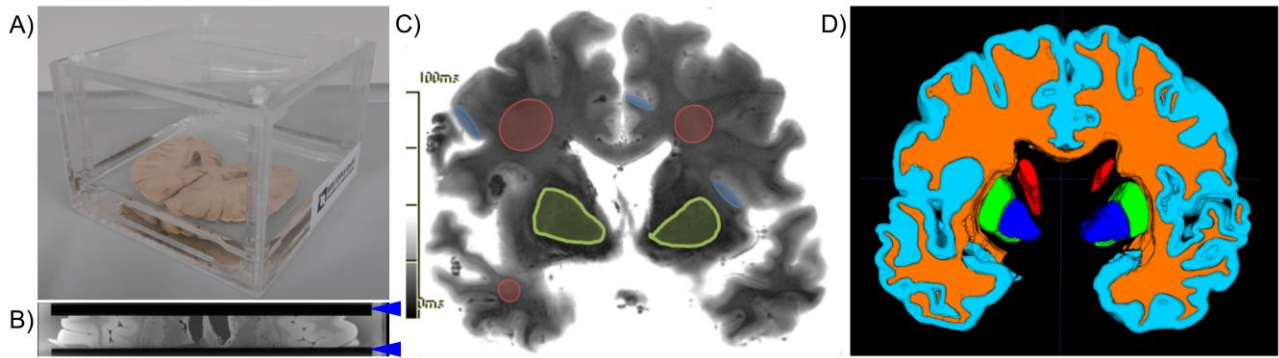


Figure 1. Setting for MR scanning

A) Brain sample fixed in a dedicated plastic container immersed in PBS; B) Axial GRE image (from the brain's coordinate reference) showing the sample fixed between two plastic plates (blue arrowheads) preventing its motion during scanning; C) repeatedly examined T_2^* map with ROIs drawn in cortex (blue), white matter (red), and lentiform nucleus (green); D) example 3D brain mask with segmented ROIs; red – caudate nucleus, dark blue – globus pallidus, green – putamen, orange – WM, light blue - cortex. Abbreviations: WM – white matter; LN – lentiform nucleus.

Signal-to-noise and contrast-to-noise ratio calculations

SNR and CNR for cortex/WM and LN/WM were calculated from high-resolution MPRAGE, early-echo GRE (GRE-TE1), and late-echo GRE (GRE-TE2) images. Early-echo GRE and MPRAGE images were chosen because proton density/ T_1 -weighted MPRAGE images had previously been shown to have strong GM/WM contrast for formalin-fixed tissue samples (11,39). Late-echo GRE was also assessed to evaluate the CNR properties from a primarily T_2^* -weighted contrast.

SNR was calculated according to the difference method (40) using:

$$SNR = \sqrt{2} \left(\frac{\text{mean signal}}{\text{noiseStd}} \right), \quad (1)$$

whereby the “mean signal” was calculated for the whole brain sample in the average of all 15 repeated measurements and the noise standard deviation (“noiseStd”) was calculated from the difference between two consecutive measurements, each with 5 averages .

For CNR calculation, 3D masks defining whole LN, WM, and cortical ROIs were segmented for each brain sample and embedding medium using ITK-SNAP (www.itksnap.org) (41). Semi-automated, active-contour segmentation mode with manual correction was used. CNR was calculated according to the difference method (40) using:

$$CNR_{12} = \sqrt{2} \left(\frac{\text{mean}(ROI_1)}{\text{noiseStd}(ROI_1)} - \frac{\text{mean}(ROI_2)}{\text{noiseStd}(ROI_2)} \right), \quad (2)$$

noting the mean signal for a given ROI was calculated as the mean intensity (across all voxels) in the average of all 15 repeated measurements; spatially concordant noise standard deviations were calculated from the difference between two consecutive measurements, each with 5 averages.

R_2^* and QSM reconstruction

T_2^* was estimated from the nonlinear fitting of multi-echo GRE data to a single-exponential decay model using a previously validated simplex-search based approach (42). In order to minimise noise-related effects, noise (standard deviation) estimates - inferred from a large (hypointense) background region - were used to

reject T_2^* -weighted signal intensities that were below a cut-off threshold of three times the estimated noise level (43). QSM reconstruction consisted of: (i) Laplacian unwrapping (44); (ii) variable spherical mean value filtering (without deconvolution) for background field removal (45) with starting kernel radius set to 25 mm (1-mm radius at the brain boundary); and (iii) non-linear morphology-enabled dipole inversion (46) with regularization parameter $\lambda=500$ (empirically optimized). The geometric average of multi-echo GRE magnitude data for each non-PBS dataset were co-registered to PBS space with a rigid-plus-nonlinear routine using ANTs v2.1 (<http://stnava.github.io/ANTs>). The resulting spatial transformations were applied to R_2^* and susceptibility maps with b-spline spatial interpolation. Subsequently, 3D ROIs including caudate nucleus (CN), putamen, globus pallidus (GP), WM, and cortex were segmented on coregistered R_2^* maps using ITK-SNAP as described above (Figure 1D). Median R_2^* and QSM values were calculated in all segmented ROIs. QSM values were normalized to a reference region in homogenous-susceptibility WM between the isocortex and the lateral ventricle.

In order to assess the effect of embedding media on deep grey matter contrast in the R_2^* and QSM quantitative maps, we calculated CNR for GP and internal capsule (IC) adopting a method described previously (47). First, GP and IC were manually segmented at the level of anterior commissure twice by the same rater. CNR was calculated using

$$CNR = \left(\frac{\text{mean}(S_1) - \text{mean}(S_0)}{\text{noiseStd}} \right), \quad (3)$$

Whereby S_1 represents the mean signal across the “union” GP mask (i.e. mask including all voxels from first and second segmentation) and S_0 represents the mean signal from the union IC mask. Noise standard deviation was calculated from voxels between GP and IC not included in either union mask.

Statistical analyses

Nonparametric repeated-measures Friedman tests and post-hoc Dunn’s multiple-comparison tests were used on the null hypothesis that there are no effects of embedding media on SNR, CNR, R_2^* , and quantitative susceptibility values. In order to further explore the impact of embedding media on quantitative MRI measurements, Z-scores were calculated across all specimens for each metric and each medium relative to the global behavior across all media. Thus, for each ROI and metric the Z-score sum for all five media was zero-centered. Data were analyzed using GraphPad Prism version 6 (GraphPad Software, Inc., San Diego, CA, USA).

Fluid-only experiment

To further characterize the embedding substances, five Falcon vials (diameter = 15 mm, length = 11 cm) were filled with PBS, neutral-buffered formalin, Galden, PBS-based agarose gel, and D_2O solutions of the same composition as those used for brain embedding. Additionally, two vials filled with ultrapure water prepared using the Milli-Q Advantage A10 water purification system (Merck, Darmstadt, Germany) were also included to serve as susceptibility references. All vials were placed in a container, embedded in 1.5% agarose gel prepared from ultrapure water (n.b. different to the PBS-based agarose solution used for post-mortem imaging), and scanned using a multi-echo 3D GRE pulse sequence with the same parameters used for brain examination, except for voxel size (i.e. voxel resolution = $0.72 \times 0.72 \times 0.72$ mm³). Subsequently, R_2^* and susceptibility maps were reconstructed with the methods described above and mean values for each embedding media were extracted from the mid-axial slice.

Neuropathological examination

Following MRI scanning, two brain slices (PM-13 and PM-14) were examined neuropathologically. Tissue blocks were collected from the frontal lobe and LN, embedded in paraffin, and sliced with a microtome into 5 μm thick sections. These slices were then stained with hematoxylin and eosin, Bielschowsky staining, 3,3'-diaminobenzidine-tetrahydrochloride (DAB) enhanced Turnbull staining for $\text{Fe}^{2+/3+}$ iron detection (48), and Luxol fast blue. Immunohistochemistry was performed using primary rabbit anti-glial fibrillary acidic protein antibodies (GFAP; dilution 1:1000; Dako, Glostrup, Denmark). For visualization of the primary antibodies, a DAKO EnVision kit[®], with peroxidase-DAB system (rabbit/mouse), was used. Sections were briefly counterstained with Mayer's hemalum solution for better visualization of cell nuclei. Experienced neuropathologists examined all stained sections to assess tissue integrity, i.e. to ensure there was no significant tissue damage resulting from the present study protocol.

Results:

Visual assessment

MPRAGE, GRE-TE1 and GRE-TE2 images showed very similar appearance and contrast for PBS, agarose, and Galden embedding (Figure 2, Figure 3, Supporting Information Figure S2). Image quality was excellent overall, though at first glance we noted formalin embedding yielded noisier images compared to other media, particularly for longer TEs. Images acquired for D_2O embedding had a slightly different appearance; they showed a contrast pattern with strong signal variations near the cortex as if D_2O had penetrated superficial regions of the cortex more readily than deep sulcal regions, deep nuclei and WM. This phenomenon also led to partial contrast reversal between cortex and WM (Figure 2, Figure 3).

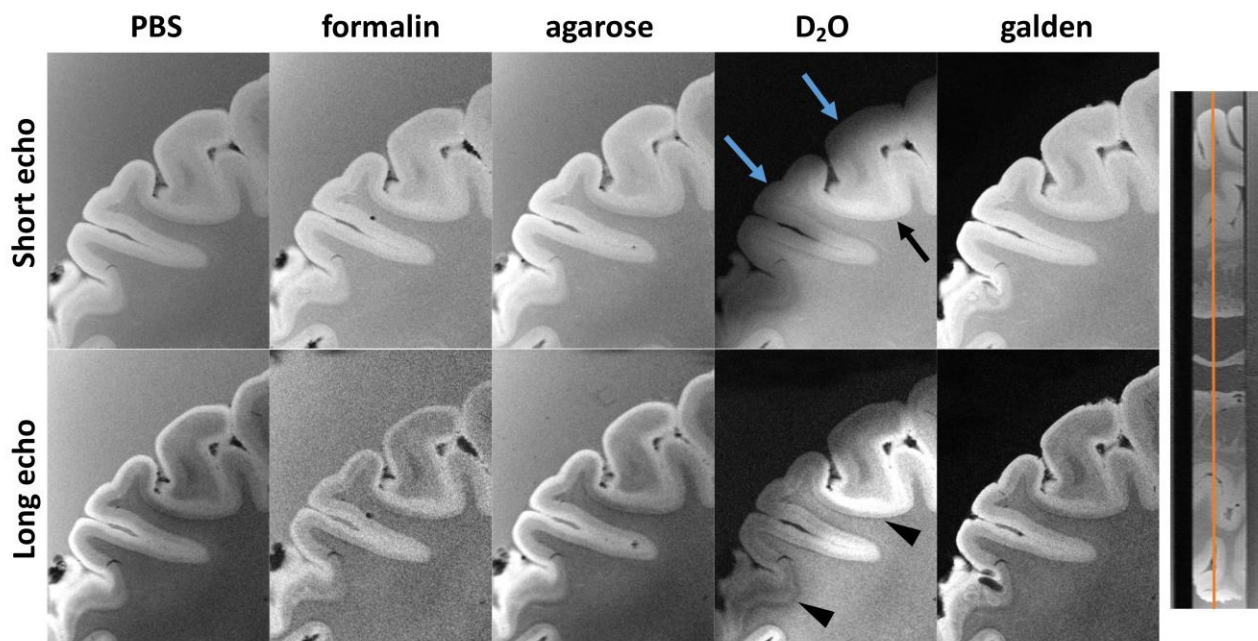


Figure 2. Visual analysis of high-resolution structural images from the specimen PM-12

Magnified views of GRE images showing cortex and white matter regions from the specimen PM-12 scanned in the different embedding media investigated; upper row depicts early-echo (TE=6.1 ms) whereas bottom row depicts late-echo (TE=19.4 ms) images. Position of the slice is indicated by orange lines in sagittal reconstructions on the right. PBS, agarose, and Galden generally yielded images with comparable SNR and grey-white matter contrast. Late echo images acquired in formalin and D_2O embedding returned lower SNR. D_2O embedding yielded images with inhomogeneous signal in the cortex due to variable penetration of the medium, low signal close to the cortical surface (blue arrow) and higher signal in deep cortical sulci (black

arrow). Additionally, D₂O enhanced the visibility of a subcortical hypointense band possibly co-localized with iron-rich subcortical u-fibers (black arrowheads).

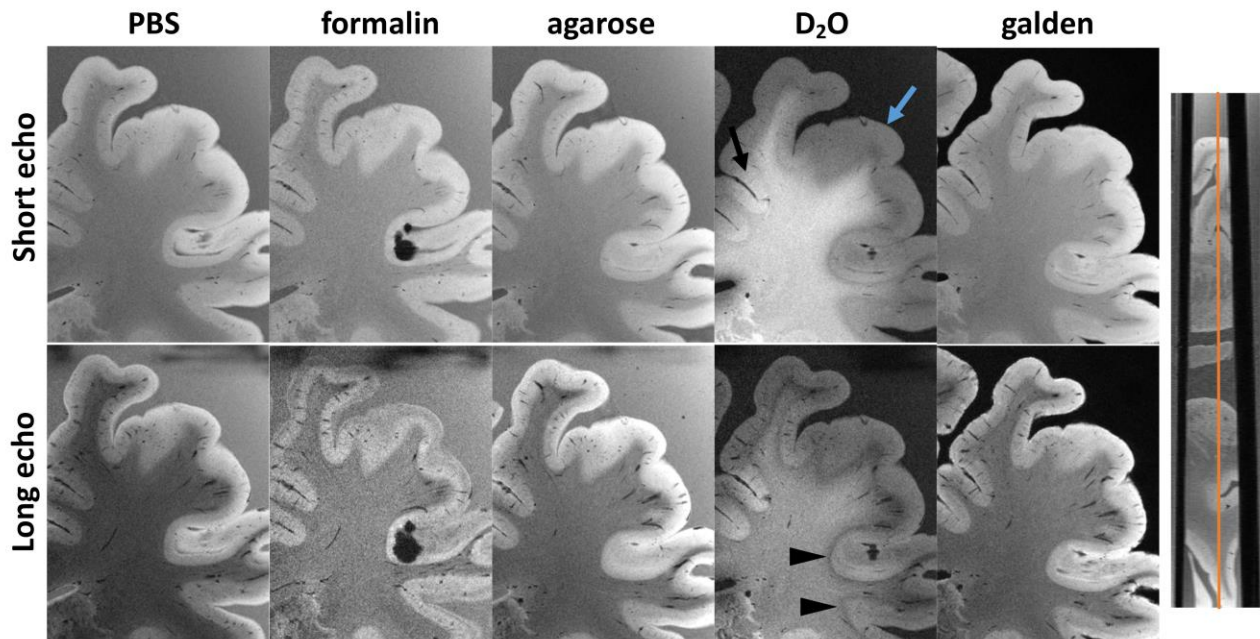


Figure 3. Visual analysis of high-resolution structural images from the specimen PM-14

Magnified views of early- (upper row) and late- (bottom row) echo GRE images showing cortex and white matter regions from the specimen PM-14 scanned in the different embedding media investigated. Position of the slice is indicated by orange lines in sagittal reconstructions on the right. Consistent with findings in specimen PM-12, late-echo images acquired in formalin and D₂O embedding returned lower SNR while D₂O embedding yielded inhomogeneous cortical signal (blue and black arrows) and prominent subcortical hypointense banding (black arrowheads).

Histopathological analysis confirmed that there were no signs of tissue damage in morphological investigation. All stainings, both histochemical and immunohistochemical, showed the expected pattern of reactivity (Supporting Information Figure S3).

SNR and CNR analysis

Since we employed the difference method for the SNR/ CNR calculation, we first assessed consistency of the signal intensity across the three measurements. We calculated the mean signal intensity in MPRAGE, GRE-TE1, and GRE-TE2 images in all consecutive measurements for each specimen and PBS embedding. The difference between measurements with highest and lowest signal intensity was 0.02 – 1.04 %. Thus, the signal is highly consistent across the measurements which renders the use of the difference method suitable for SNR/ CNR calculations.

Significant SNR differences across embedding media were observed for MPRAGE ($p=0.02$), GRE-TE1 ($p=0.008$), and GRE-TE2 data ($p=0.04$). Generally, the highest SNRs were measured for GRE-TE1 images (Table 2, Supporting Information Figure S4). Overall the highest SNR Z-scores were obtained for agarose and PBS embedding, and the lowest for D₂O (Figure 3).

		PBS	Formalin	Agarose	D ₂ O	Galden	P value
SNR	MPRAGE	16.0 (1.7)	15.0 (3.4)	15.6 (1.1)	11.5 (2.3)	14.9 (2.7)	0.020*
	GRE-TE1	20.4 (2.6)	17.8 (2.5)	20.3 (1.2)	14.0 (5.6)	19.0 (3.4)	0.008**
	GRE-TE2	10.7 (1.6)	7.8 (1.6)	12.0 (3.3)	7.9 (2.7)	10.8 (3.8)	0.034
CNR cortex-WM	MPRAGE	4.8 (2.5)	2.8 (2.1)	4.3 (2.7)	5.0 (0.7)	4.0 (1.9)	0.230
	GRE-TE1	8.0 (2.3)	5.0 (0.8)	8.5 (3.3)	4.0 (2.5)	6.7 (1.8)	0.039
	GRE-TE2	7.9 (2.1)	2.5 (1.0)	7.8 (4.2)	0.3 (1.4)	4.7 (2.9)	0.001**
CNR LN-WM	MPRAGE	0.5 (1.2)	0.9 (1.2)	1.5 (1.9)	0.6 (2.0)	1.0 (1.2)	0.260
	GRE-TE1	1.9 (3.4)	2.1 (3.1)	2.3 (3.8)	3.0 (3.6)	2.5 (3.0)	0.326
	GRE-TE2	1.7 (2.9)	1.4 (3.0)	3.2 (2.6)	3.0 (5.3)	3.0 (2.8)	0.134

Results of post-hoc tests: * D2O vs PBS significant; ** D2O vs PBS; D2O vs agarose significant

Abbreviations: SNR= signal-to-noise ratio; CNR= contrast-to-noise ratio; WM= white matter; LN= lentiform nucleus.

CNRs between cortex and WM, and between LN and WM were generally higher for GRE than MPRAGE (Table2, Supporting Information Figure S4). Cortex/WM CNRs on MPRAGE images did not greatly differ for any particular embedding media. However, significant differences were identified for GRE-TE1 ($p=0.04$) and GRE-TE2 data ($p=0.002$). For GRE data, cortex/WM CNR Z-scores were consistently higher when using PBS and agarose embedding, whereas systematically lower Z-score values were observed for formalin and D₂O – a pattern most pronounced in late-echo GRE images (Figure 4). Regarding LN/WM CNRs, no significant differences were observed for MPRAGE or GRE data.

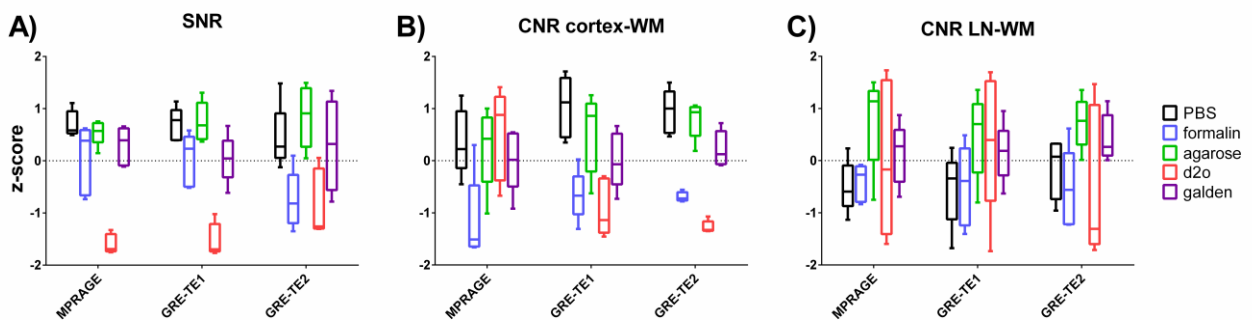


Figure 4. Signal-to-noise and contrast-to-noise ratio Z-statistics

Z-scores of A) SNR, and B) CNR between cortex and white matter and C) CNR between lentiform nucleus and white matter calculated for each medium relative to the global behavior across all media for a given specimen and MR image type.

Effect of embedding media on post-mortem R_2^* and QSM

From a qualitative standpoint, R_2^* and QSM were overall satisfactory across embedding media (Figure 5). We noted, however, intersubject variability of median R_2^* values was greater in the basal ganglia than in WM or

cortex (Table 3, Figure 6A, Supporting Information Table S1). There were no significant deep grey matter CNR differences in R_2^* parametric maps across embedding media ($p=0.94$) while significant differences were found for QSM ($p=0.002$); specifically, the lowest deep grey matter CNRs in QSM were observed for D_2O and formalin embedding, and the highest for agarose and galden embedding (Supporting Information Figure S5).

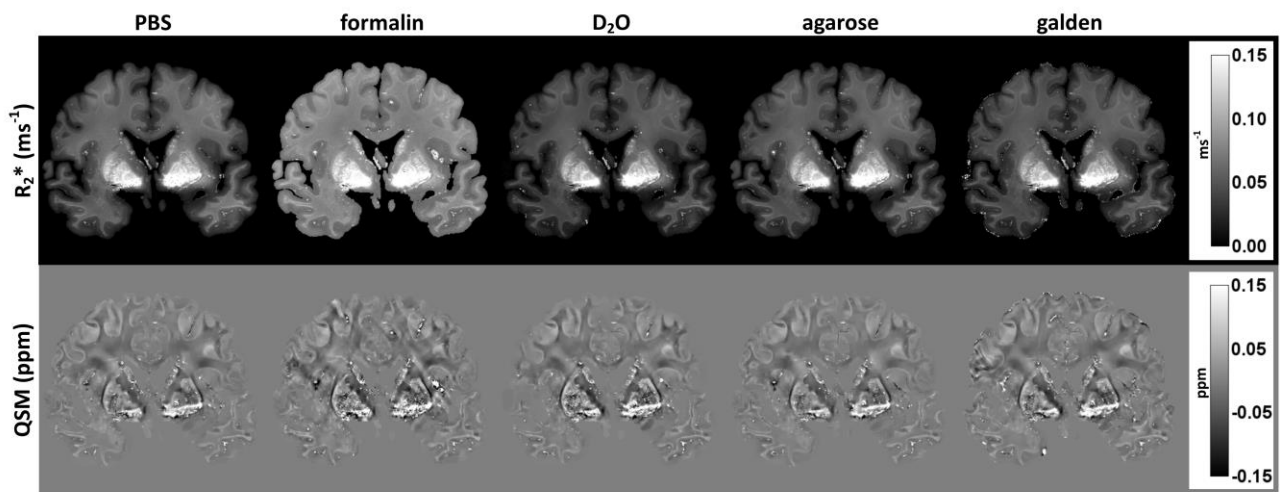


Figure 5. Quantitative MRI

Example of quantitative R_2^* (upper row) and susceptibility (bottom row) maps obtained using different embedding media.

Table 3. Comparison of median (IQR) R_2^* and susceptibility values in different ROIs and embedding media						
	PBS	Formalin	Agarose	D2O	Galden	P value
R_2^* (ms^{-1})						
GP	0.121 (0.037)	0.122 (0.051)	0.116 (0.041)	0.118 (0.031)	0.116 (0.040)	0.002*
Putamen	0.092 (0.028)	0.094 (0.033)	0.081 (0.033)	0.078 (0.024)	0.082 (0.030)	0.002*
Caudate	0.071 (0.025)	0.077 (0.026)	0.063 (0.032)	0.059 (0.027)	0.066 (0.029)	0.003*
WM	0.062 (0.010)	0.075 (0.021)	0.049 (0.007)	0.048 (0.010)	0.049 (0.005)	0.003*
Cortex	0.037 (0.008)	0.067 (0.017)	0.031 (0.004)	0.028 (0.007)	0.032 (0.007)	0.004*
Susceptibility (ppm)						
GP	0.035 (0.025)	0.042 (0.036)	0.021 (0.017)	0.028 (0.022)	0.031 (0.027)	0.326
Putamen	0.019 (0.020)	0.009 (0.034)	0.013 (0.013)	0.025 (0.016)	0.019 (0.024)	0.275
Caudate	0.014 (0.015)	0.009 (0.027)	0.010 (0.015)	0.015 (0.019)	0.009 (0.027)	0.451
WM	0.007 (0.006)	0.000 (0.016)	0.002 (0.013)	0.008 (0.005)	0.003 (0.011)	0.692
Cortex	0.004 (0.006)	0.002 (0.015)	0.001 (0.014)	0.009 (0.005)	0.002 (0.012)	0.525
Results of post-hoc tests: * formalin vs agarose significant; formalin vs D2O significant						

Quantitatively, we identified significant R_2^* differences across embedding media for all ROIs investigated, i.e. GP ($p=0.002$), putamen ($p=0.002$), CN ($p=0.003$), WM ($p=0.003$), and cortex ($p=0.004$). On post-hoc investigation, R_2^* Z-scores were found to be systematically higher for formalin embedding compared to all other media. In addition, PBS Z-scores were also higher than those for agarose, D₂O and Galden embedding, except in the cortex (Figure 6B).

No significant differences in bulk susceptibility were observed across embedding media (Table 3, Figure 6C). Mean QSM Z-scores for formalin, in contrast to those for R_2^* , were not systematically different to mean Z-scores for other embedding media. Though we noted regional variance and intersubject variability were overall greater for QSM than for R_2^* (Supporting Information Table S2) and found, in addition, QSM Z-score dispersions for formalin and agarose that were consistently larger than those for PBS, Galden and D₂O (Figure 6D).

A final observation from Z-statistics of both R_2^* and QSM is that PBS embedding rarely yielded extreme values (Figure 6B,D).

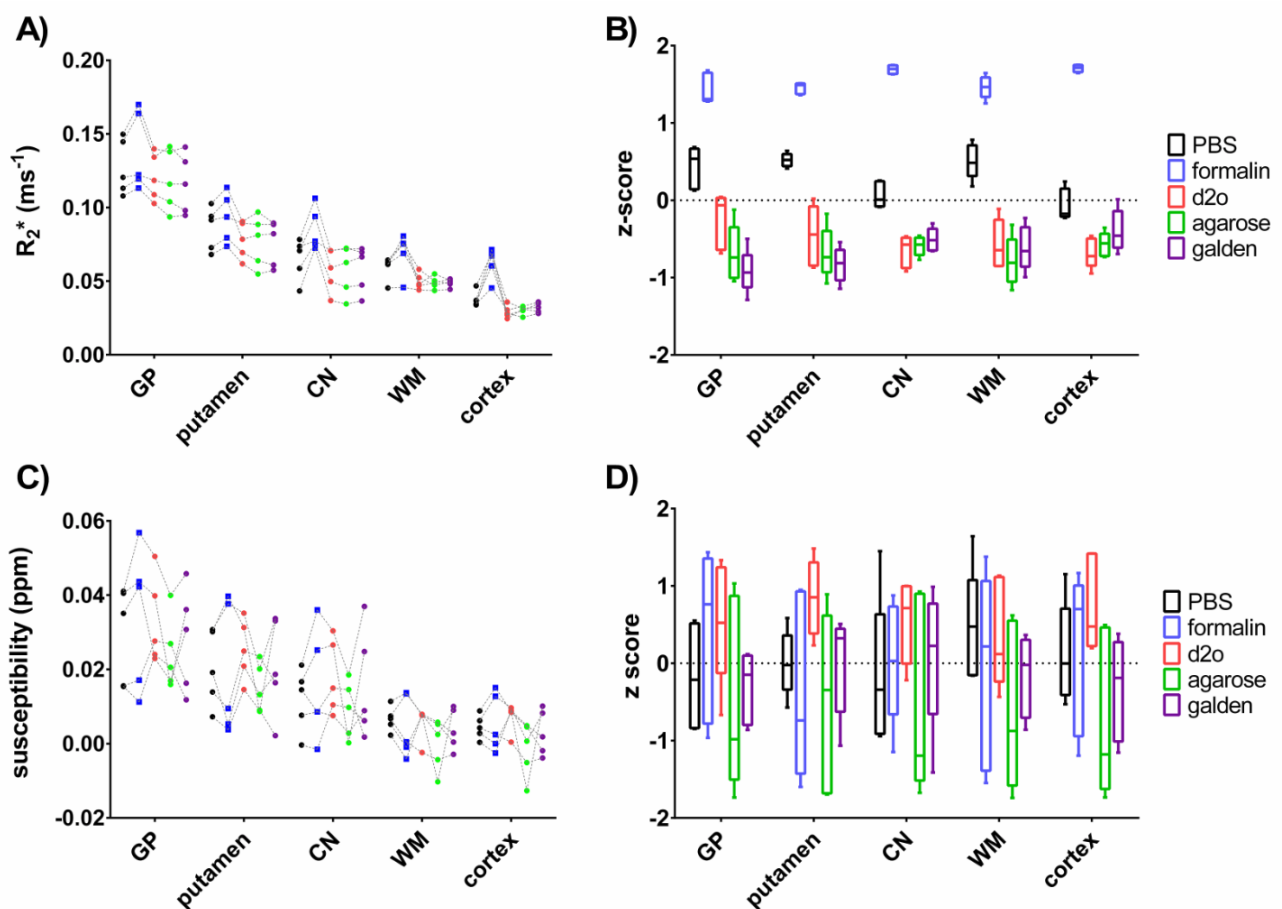


Figure 6. R_2^* relaxometry and QSM analysis

Median A) R_2^* values (ms^{-1}) and C) susceptibility values measured for different embedding media. Values for each specimen's ROIs are connected by dotted lines; B) R_2^* and D) QSM Z-scores calculated for each medium relative to the global behavior across specimens and for each embedding medium and ROI.

Temperature monitoring confirmed stable thermal conditions during these quantitative measurements. The minimum and maximum temperatures recorded across all experiments were 24.8°C and 28.2°C, respectively.

Media characterization

Formalin solution (phosphate-buffered) returned the highest R_2^* relaxivity values of all media types, although notably, this was not mirrored by a relative increase in absolute susceptibility. PBS and agarose – both also containing phosphate ions – were found to be more diamagnetic than ultrapure water, with agarose yielding the most negative susceptibilities. R_2^* estimates for PBS were similar to those for ultrapure water, whereas agarose exhibited relatively strong R_2^* relaxivity (compared to PBS and ultrapure water) conceivably due to its strong diamagnetism (Figure 7). Galden and D_2O have a proton-free composition, hence precluding reliable R_2^* and QSM calculations for these media. The non-local nature of MR-phase based field offsets (from which QSM is derived), however, may provide indirect qualitative information about the extent of local dipole fields around the vials (n.b. these are cylindrical vials largely aligned with the main field, hence only highly diamagnetic or paramagnetic substances would be expected to yield a detectable frequency shift around the vial). On visual inspection, we found local field offsets surrounding Galden and D_2O vials that were relatively weak compared to field behaviours around PBS and agarose tubes, suggesting Galden and D_2O are neither strongly diamagnetic nor strongly paramagnetic (Figure 7). Quantitative QSM/ R_2^* estimates for all samples are summarised in Supporting Information Table S3.

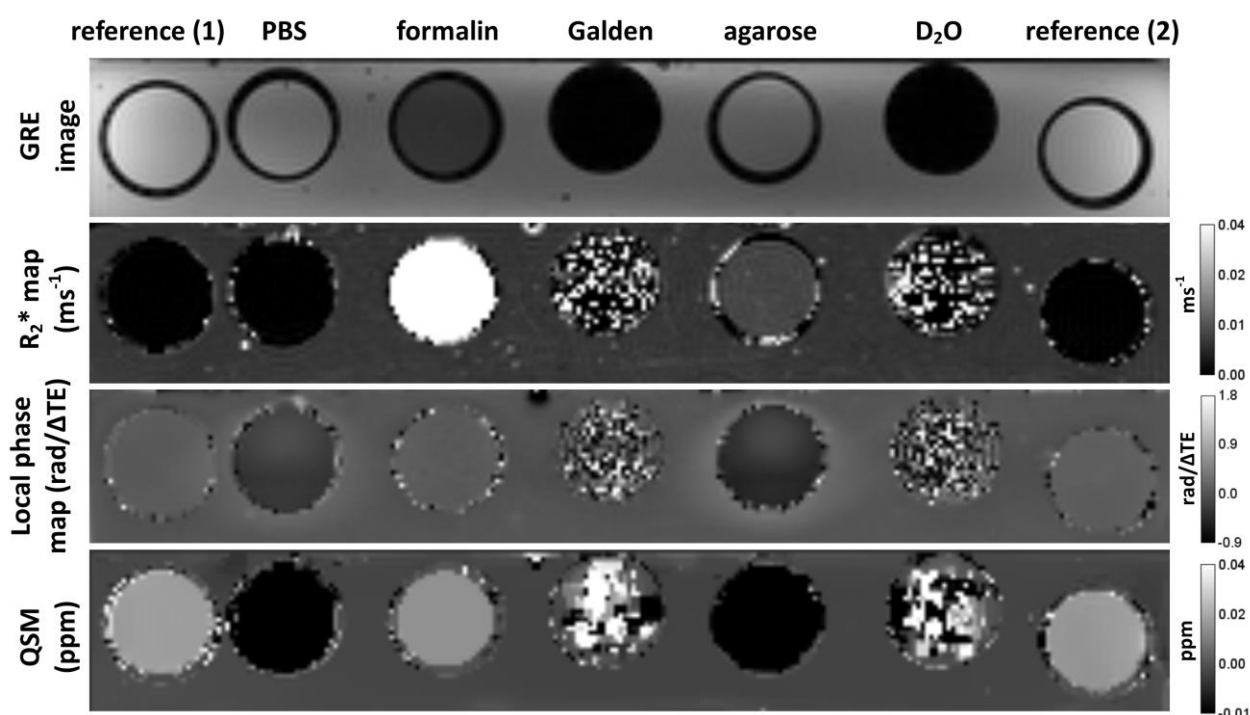


Figure 7. Fluid-only data

T_2^* -weighted GRE image (upper row), quantitative R_2^* (upper middle row), local phase map (bottom middle row), and quantitative susceptibility maps (bottom row) for seven vials, five containing the different embedding media and two ultra-pure water references. We found Galden and D_2O returned no MR signal; R_2^* and susceptibility, therefore, could not be quantified. Formalin had the highest R_2^* relaxivity of all media from which we could obtain a reliable estimate. Bulk susceptibility for formalin was higher than that for PBS and agarose but comparable to that for the water reference. Agarose returned slightly more diamagnetic susceptibility (mirrored by higher R_2^* relaxivity) than PBS.

Discussion:

The primary aim of this study was to compare the effects of embedding media on high-resolution structural imaging and quantitative R_2^*/QSM MRI measurements from formalin-fixed brain slices commonly stored in

brain banks. These specimens are frequently subject to *post-mortem* MRI examination using the above mentioned techniques e.g. for detection of cortical lesions in multiple sclerosis (49), microinfarcts (5), or microbleeds (32,50). Herein, we found direct evidence that the choice of embedding medium can affect image quality, contrast, and quantitative readouts from gradient-echo based MR microscopy (for summary see Supporting Information Table S4). Notably, formalin embedding increased tissue R_2^* leading to SNR starvation for long echo-time acquisitions. D_2O embedding also yielded images with low SNR, and visually tractable contrast differences between cortex and WM for all scan types. Overall SNR and cortex/WM contrast in GRE images were greatest for PBS and agarose embedding, whereas the LN/WM contrast appeared to be largely independent of embedding media. No statistical effect of embedding media was identified on bulk susceptibility measurements, though QSM variance was notably higher than that for R_2^* particularly for formalin and agarose.

Qualitatively, short echo time, low flip angle (i.e. proton density weighted) GRE imaging yielded more homogeneous contrast properties for PBS, agarose, and Galden embedding than for D_2O and (to a lesser extent) formalin (see Figures 2 and 3). Similar image quality from these three substances was an expected result on the basis that Galden and agarose are largely non-penetrating agents, i.e. technically therefore samples were soaked in PBS. In fact, image quality was generally satisfactory for all PBS-washed formalin-fixed specimens embedded in non-penetrating media. In contrast, idiosyncratic behaviour was observed for D_2O embedding, i.e. reduced SNR, particularly in the cortex, and reversed cortex/WM contrast possibly driven by poor D_2O penetration in WM, which also led to marked subcortical hypointensity banding most apparent at sulcal walls (see Figures 2 and 3). This pattern might have been related to uneven diffusional alterations during the fixation process. It was previously shown that brain tissue fixation renders cortical diffusion coefficients to be much higher than those in WM (19), supporting a hypothesis of preferential D_2O /PBS exchange in the cortex. It is also conceivable that the dark banding observed for D_2O embedding at the cortical-WM interface might reflect deep cortical layers or subcortical U-fibres with much lower fractional anisotropies than those in adjacent tissue (33). Overall, sample penetration with D_2O was incomplete and inhomogenous, suggesting that much longer soaking times are required to achieve a more stable imaging behaviour with D_2O embedding.

In agreement with qualitative observations, PBS and agarose embedding returned the greatest cortex/WM GRE contrast differences, whereas the lowest CNRs were measured with formalin and D_2O embedding (see Figure 4). In contrast, we did not observe significant lenticular nucleus/WM CNR differences. The present results also suggest that the superficial cortex, which is in direct contact with the embedding medium, is thus more vulnerable to differential medium-related effects.

The assessment of SNR and CNR characteristics across different embedding media was a major focus in the present study. We must note there are other methods that could have further increased image SNR, e.g. adding gadolinium to the embedding medium and/or increasing sample temperature (19). The latter approach for example has been shown to increase diffusivity along with a disproportionate T_2 increase (16), hence boosting image SNR. These techniques, however, are beyond the scope of this study and would require a separate calibration.

Turning to R_2^* and QSM, the present study investigated parametric maps that were overall in agreement with known patterns of tissue iron concentration in the human brain (51), i.e. ROIs were assorted from the highest to lowest R_2^* and QSM as follows: GP, putamen, CN, WM, and cortex. In addition, higher intersubject variability of R_2^* /QSM measurements was observed for basal ganglia compared to WM and cortex, presumably due to heterogenous age-related iron deposition (52). Despite the effects of embedding media on the SNR and CNR of GRE images, the overall quality and CNR of deep grey matter nuclei in R_2^* parametric maps were similar irrespective of embedding medium used. The most striking finding was a systematic R_2^*

increase (across all ROIs) when using formalin embedding. This effect was not apparent on QSM (see Figure 5), although a potentially short- T_2^* (i.e. low SNR) related increase in QSM variance was observed. Consequently, CNR of the deep grey matter in QSM images was mildly but significantly decreased for formalin and D_2O embedding (see Supporting Information Figure S5). It has previously been shown that adding 4% formaldehyde to PBS markedly shortens T_2 relaxation (53), and that washing out bulk fixative from thin rat cortical slices (fixed for approximately ten days) restores T_2 relaxation times to typical *in vivo* values (14). It has also been suggested that different brands of formalin solution might exhibit differential magnetostatic properties (54). Conceivably, thus, the strong paramagnetic moments observed in some - but not all - formalin preparations might not originate from formaldehyde but from other chemical substances present in the mixture. Our results were consistent with previous findings in that we also observed a steep reduction in R_2^* after washing out formalin with PBS which was, however, not accompanied by a corresponding QSM offset, but by a decrease in QSM variability. These results are partially consistent with another study that found no effect of formalin fixation on bulk tissue susceptibility (55). These observations, supported by results from our vial experiment (see Figure 7 and Supporting Information Table S3), suggest that the short- T_2^* behaviour of the formalin solution used in the present study might not have been driven by its magnetostatic properties alone. An alternative explanation, supported by a previous microwave spectroscopy study (56), is that the formaldehyde molecule has counteracting paramagnetic and diamagnetic components at the microscopic level, though this is only a hypothesis at present time. Of note, the formaldehyde solution used in our experiment was phosphate-buffered, i.e. it contained phosphate ions such as those in PBS (which in turn returned a strong diamagnetic effect). It might be conceivable that the field induced by phosphate ions might have attenuated/reversed a potential paramagnetic moment from formaldehyde. Therefore, whether formalin R_2^* increase is driven by T_2 , susceptibility effects, or a combination of both remains unclear and warrants further investigation.

A step-wise R_2^* reduction when imaging with agarose, Galden and D_2O embedding compared to formalin and PBS (see Figure 6A,B) suggests that bulk formalin may have been incompletely removed, i.e. its washing out could have continued after imaging with PBS – particularly in WM but also other deep structures. In contrast, cortical R_2^* values were more stable and similar in absolute terms to those observed *in vivo* (57), suggesting formaldehyde had been completely washed out from cortical regions prior to PBS scanning. In WM, putamen and CN, however, R_2^* across all media was 20-30% greater compared to *in vivo* conditions. This could be due to a number of factors including post-mortem structural tissue changes, lower specimen temperature compared to *in vivo* conditions, additive chemical reactions in the fixative agent that are independent on bulk formalin (58), or incomplete clearance resulting from slow exchange of soaking fluid in regions of low diffusivity. Study by Birkl et al. indicated no significant differences in R_2^* between *in vivo* and “fresh” unfixed brain specimens while R_2^* increased by approximately 30% in cortex, WM, basal ganglia, and thalamus after formalin fixation; it further increased when temperature was lower than *in vivo* (16). Based on these results, we think it is unlikely that the R_2^* difference observed between unfixed and fixed tissue could be due to post mortem structural tissue changes. Of note, we deliberately chose post mortem intervals in the range of 10-80 hours as these intervals are not uncommon for samples stored in biobanks (59,60). To ensure usage of fit tissue, we included only samples from corpses that were kept in a cooling box before sectioning and showing no signs of tissue damage or lysis on a thorough examination performed by experienced neuropathologists. Of all embedding media investigated in the present study, only D_2O had an expected osmolarity gradient from tissue to fluid, which may have caused osmotic influx from the embedding medium to the specimen. By diluting the remaining free fixative, osmotic influx may have further reduced tissue R_2^* (27). Such an effect could explain the relatively small R_2^* values detected when using D_2O in cortex and CN, i.e. in areas directly adjacent to the embedding substance. It is known from the literature (16) that T_2^* relaxation time measurements in structures with paramagnetic behavior are affected by temperature. A

temperature increase of $\Delta T=1^{\circ}\text{C}$ increases the T_2^* relaxation time by 0.2 ms at 3T. Taking this into account, the peak temperature variation of $\Delta T=3^{\circ}\text{C}$ observed in our experiments would shift the T_2^* relaxation time by a maximum of 0.6 ms, which is unlikely to bias our results.”

In summary, the present results confirmed T_2^* shortening due to residual formaldehyde which leads to SNR and CNR loss in GRE imaging. These results discourage the use of formalin as embedding medium for high-resolution anatomical imaging, and highlight the paramount importance of appropriately washing out the fixative agent prior to MRI scanning. It must be emphasised that full penetration of embedding fluid into a large formalin-fixed specimen containing tissues with different diffusion properties is a lengthy and dynamic process. A previous imaging study using fixed macaque brain tissue and PBS with gadolinium, for example, confirmed rapid equilibrium across the cortex but much slower penetration (incomplete after three weeks) in deeper brain regions (19).

Regarding QSM, the present study identified greater intraregional and intersubject variability than for R_2^* , particularly when using formalin and agarose embedding, but no systematic offsets were observed other than a slight trend towards low susceptibility values for agarose (see Figure 6C,D). Fluid-only measurements revealed that our PBS-based agarose solution is more diamagnetic than pure water, which could explain the markedly high R_2^* and slightly negative QSM bias (accompanied by relatively large QSM dispersion) on *post mortem* measurements when using agarose embedding.

Several study limitations are worth discussing. First, experiments on specimens outside the influence of a fixative agent were deliberately limited to seven days. Such time constraint may have led to incomplete tissue penetration (19), particularly for D_2O – an aspect of crucial importance when studying larger samples (33). It is worth emphasising that quantitative estimates from *post mortem* MRI might be affected by many experimental factors including post-mortem interval, fixation method, fixation times, sample size and temperature. In our study, we were interested in substantial effects of embedding media. For this reason we did not use strictly uniform post-mortem intervals, fixation times and source of samples. Due to this approach and owing to the relatively low number of examined samples, it is possible that our study might not have enough power to detect other minor effects of embedding media. It is also recognized that RF inhomogeneities on the MPRAGE images acquired using D_2O immersion might have an effect on our results due to the low conductivity/high permittivity of the medium.

Therefore, a note of caution for future investigations is that the present results should not be directly extrapolated to every scanning condition, e.g. whole human brains or hemispheres, or brain slices that were stored in formalin for many years, as this might result in severe inconsistencies with the results from this study. In addition, it is worth noting that due to time constraints, our study had to focus on a limited number of MRI parameters. Future work is warranted to extend this work to R_1 relaxometry, diffusion and magnetization transfer measurements, which may also vary with different types of embedding.

In conclusion, we showed that the choice of embedding medium affects image contrast and quantitative GRE-based 7.0 T MRI measurements of *post mortem* brain tissue. PBS, agarose, and Galden have no major disadvantages and can be postulated as appropriate multi-purpose media, though we saw slight indications that PBS-based GRE microscopy might be the most stable overall. Formalin embedding, although convenient for fixed-tissue imaging, was found to significantly shorten T_2^* relaxation times, hence limiting its use in this context, and not recommended for direct comparison with *in vivo* values. A potential application for formalin embedding, however, might be its use e.g. in group studies using large specimens where preventing biases due to incomplete washing out of bulk formalin is of utmost importance. Finally, it is worth pointing out that despite the promise of D_2O as an alternative proton-free medium, we did not find this to represent a suitable

embedding medium for the present experimental conditions. Whether D₂O embedding might have any advantage over longer washout periods or using smaller tissue samples remains to be determined.

Acknowledgements:

This study was supported by Czech Ministry of Health (grant number 15-25602A and conceptual development of research organization 64165, General University Hospital in Prague), by Charles University (Project Progres Q27/LF1 and Q28/LF1) and by OPPK (CZ.2.16/3.1.00/24509). T.N. was supported by the Helmholtz Alliance ICEMED - Imaging and Curing Environmental Metabolic Diseases, through the Initiative and Network Fund of the Helmholtz Association (ICEMED-Project 1210251). The Wellcome Centre for Human Neuroimaging is supported by core funding from the Wellcome (203147/Z/16/Z).

References:

1. Nagara H, Inoue T, Koga T, Kitaguchi T, Tateishi J, Goto I. Formalin fixed brains are useful for magnetic resonance imaging (MRI) study. *J Neurol Sci* 1987;81(1):67-77.
2. Boyko OB, Alston SR, Fuller GN, Hulette CM, Johnson GA, Burger PC. Utility of postmortem magnetic resonance imaging in clinical neuropathology. *Arch Pathol Lab Med* 1994;118(3):219-225.
3. Ruder TD, Thali MJ, Hatch GM. Essentials of forensic post-mortem MR imaging in adults. *Br J Radiol* 2014;87(1036):20130567.
4. Reeves C, Tachrount M, Thomas D, Michalak Z, Liu J, Ellis M, Diehl B, Misericocchi A, McEvoy AW, Eriksson S, Yousry T, Thom M. Combined Ex Vivo 9.4T MRI and Quantitative Histopathological Study in Normal and Pathological Neocortical Resections in Focal Epilepsy. *Brain Pathol* 2016;26(3):319-333.
5. van Veluw SJ, Zwanenburg JJ, Rozemuller AJ, Luijten PR, Spliet WG, Biessels GJ. The spectrum of MR detectable cortical microinfarcts: a classification study with 7-tesla postmortem MRI and histopathology. *J Cereb Blood Flow Metab* 2015;35(4):676-683.
6. Langkammer C, Schweser F, Krebs N, Deistung A, Goessler W, Scheurer E, Sommer K, Reishofer G, Yen K, Fazekas F, Ropele S, Reichenbach JR. Quantitative susceptibility mapping (QSM) as a means to measure brain iron? A post mortem validation study. *Neuroimage* 2012;62(3):1593-1599.
7. Langkammer C, Krebs N, Goessler W, Scheurer E, Ebner F, Yen K, Fazekas F, Ropele S. Quantitative MR imaging of brain iron: a postmortem validation study. *Radiology* 2010;257(2):455-462.
8. Seehaus AK, Roebroek A, Chiry O, Kim DS, Ronen I, Bratzke H, Goebel R, Galuske RA. Histological validation of DW-MRI tractography in human postmortem tissue. *Cereb Cortex* 2013;23(2):442-450.
9. Keren NI, Taheri S, Vazey EM, Morgan PS, Granholm AC, Aston-Jones GS, Eckert MA. Histologic validation of locus coeruleus MRI contrast in post-mortem tissue. *Neuroimage* 2015;113:235-245.
10. Fatterpekar GM, Naidich TP, Delman BN, Aguinaldo JG, Gultekin SH, Sherwood CC, Hof PR, Drayer BP, Fayad ZA. Cytoarchitecture of the human cerebral cortex: MR microscopy of excised specimens at 9.4 Tesla. *AJNR Am J Neuroradiol* 2002;23(8):1313-1321.
11. Pfefferbaum A, Sullivan EV, Adalsteinsson E, Garrick T, Harper C. Postmortem MR imaging of formalin-fixed human brain. *Neuroimage* 2004;21(4):1585-1595.
12. Zeineh MM, Chen Y, Kitzler HH, Hammond R, Vogel H, Rutt BK. Activated iron-containing microglia in the human hippocampus identified by magnetic resonance imaging in Alzheimer disease. *Neurobiol Aging* 2015;36(9):2483-2500.

13. Dal-Bianco A, Grabner G, Kronnerwetter C, Weber M, Hoftberger R, Berger T, Auff E, Leutmezer F, Trattinig S, Lassmann H, Bagnato F, Hametner S. Slow expansion of multiple sclerosis iron rim lesions: pathology and 7 T magnetic resonance imaging. *Acta Neuropathol* 2017;133(1):25-42.
14. Shepherd TM, Thelwall PE, Stanisiz GJ, Blackband SJ. Aldehyde fixative solutions alter the water relaxation and diffusion properties of nervous tissue. *Magn Reson Med* 2009;62(1):26-34.
15. Shepherd TM, Flint JJ, Thelwall PE, Stanisiz GJ, Mareci TH, Yachnis AT, Blackband SJ. Postmortem interval alters the water relaxation and diffusion properties of rat nervous tissue--implications for MRI studies of human autopsy samples. *Neuroimage* 2009;44(3):820-826.
16. Birkl C, Langkammer C, Golob-Schwarzl N, Leoni M, Haybaeck J, Goessler W, Fazekas F, Ropele S. Effects of formalin fixation and temperature on MR relaxation times in the human brain. *NMR Biomed* 2016;29(4):458-465.
17. Sun SW, Neil JJ, Liang HF, He YY, Schmidt RE, Hsu CY, Song SK. Formalin fixation alters water diffusion coefficient magnitude but not anisotropy in infarcted brain. *Magn Reson Med* 2005;53(6):1447-1451.
18. Sun SW, Neil JJ, Song SK. Relative indices of water diffusion anisotropy are equivalent in live and formalin-fixed mouse brains. *Magn Reson Med* 2003;50(4):743-748.
19. D'Arceuil HE, Westmoreland S, de Crespigny AJ. An approach to high resolution diffusion tensor imaging in fixed primate brain. *Neuroimage* 2007;35(2):553-565.
20. Thickman DI, Kundel HL, Wolf G. Nuclear magnetic resonance characteristics of fresh and fixed tissue: the effect of elapsed time. *Radiology* 1983;148(1):183-185.
21. Kamman RL, Go KG, Stomp GP, Hulstaert CE, Berendsen HJ. Changes of relaxation times T1 and T2 in rat tissues after biopsy and fixation. *Magn Reson Imaging* 1985;3(3):245-250.
22. Shatil AS, Uddin MN, Matsuda KM, Figley CR. Quantitative Ex Vivo MRI Changes due to Progressive Formalin Fixation in Whole Human Brain Specimens: Longitudinal Characterization of Diffusion, Relaxometry, and Myelin Water Fraction Measurements at 3T. *Front Med (Lausanne)* 2018;5:31.
23. Tovi M, Ericsson A. Measurements of T1 and T2 over time in formalin-fixed human whole-brain specimens. *Acta Radiol* 1992;33(5):400-404.
24. Blamire AM, Rowe JG, Styles P, McDonald B. Optimising imaging parameters for post mortem MR imaging of the human brain. *Acta Radiol* 1999;40(6):593-597.
25. Dawe RJ, Bennett DA, Schneider JA, Vasireddi SK, Arfanakis K. Postmortem MRI of human brain hemispheres: T2 relaxation times during formaldehyde fixation. *Magn Reson Med* 2009;61(4):810-818.
26. Yong-Hing CJ, Obenaus A, Stryker R, Tong K, Sarty GE. Magnetic resonance imaging and mathematical modeling of progressive formalin fixation of the human brain. *Magn Reson Med* 2005;54(2):324-332.
27. Hales PW, Burton RA, Bollensdorff C, Mason F, Bishop M, Gavaghan D, Kohl P, Schneider JE. Progressive changes in T(1), T(2) and left-ventricular histo-architecture in the fixed and embedded rat heart. *NMR Biomed* 2011;24(7):836-843.
28. van Veluw SJ, Biessels GJ, Luijten PR, Zwanenburg JJ. Assessing Cortical Cerebral Microinfarcts on High Resolution MR Images. *J Vis Exp* 2015(105).
29. Guilfoyle DN, Helpert JA, Lim KO. Diffusion tensor imaging in fixed brain tissue at 7.0 T. *NMR Biomed* 2003;16(2):77-81.
30. Plantinga BR, Roebroek A, Kemper VG, Uludag K, Melse M, Mai J, Kuijf ML, Herrler A, Jahanshahi A, Ter Haar Romeny BM, Temel Y. Ultra-High Field MRI Post Mortem Structural Connectivity of the Human Subthalamic Nucleus, Substantia Nigra, and Globus Pallidus. *Front Neuroanat* 2016;10:66.
31. Birkl C, Langkammer C, Krenn H, Goessler W, Ernst C, Haybaeck J, Stollberger R, Fazekas F, Ropele S. Iron mapping using the temperature dependency of the magnetic susceptibility. *Magn Reson Med* 2015;73(3):1282-1288.

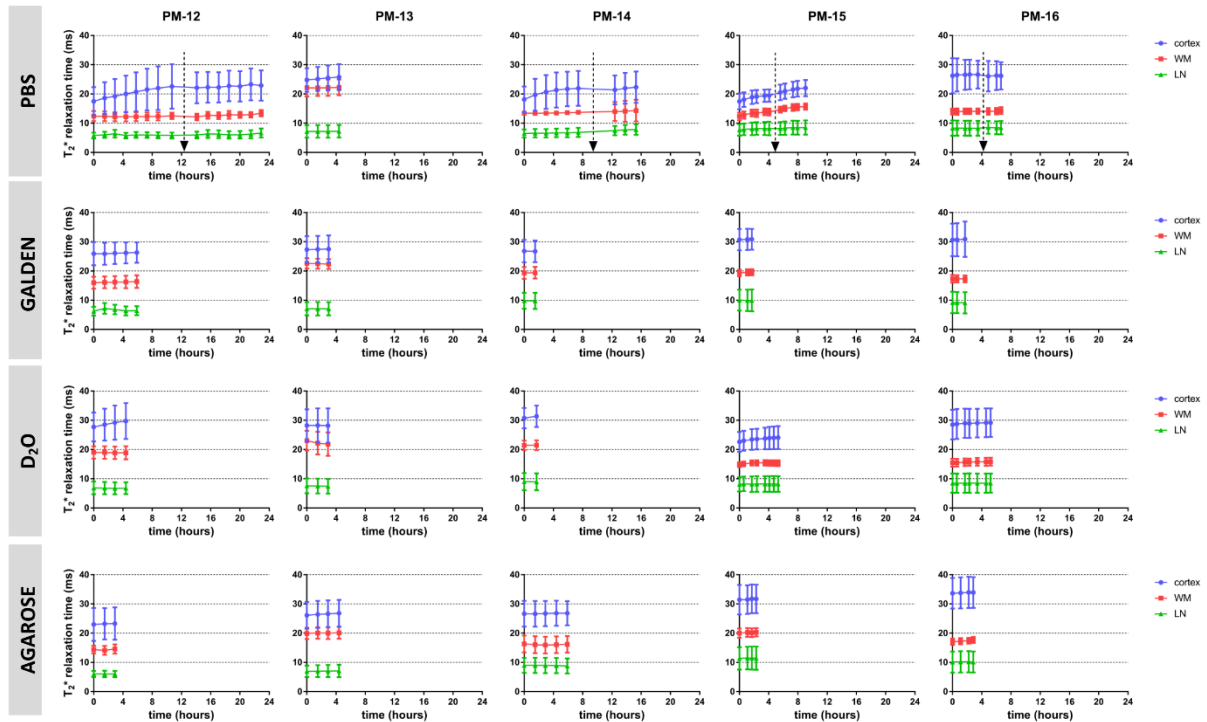
32. Janaway BM, Simpson JE, Hoggard N, Highley JR, Forster G, Drew D, Gebril OH, Matthews FE, Brayne C, Wharton SB, Ince PG, Function MRCC, Ageing Neuropathology S. Brain haemosiderin in older people: pathological evidence for an ischaemic origin of magnetic resonance imaging (MRI) microbleeds. *Neuropathol Appl Neurobiol* 2014;40(3):258-269.
33. Miller KL, Stagg CJ, Douaud G, Jbabdi S, Smith SM, Behrens TE, Jenkinson M, Chance SA, Esiri MM, Voets NL, Jenkinson N, Aziz TZ, Turner MR, Johansen-Berg H, McNab JA. Diffusion imaging of whole, post-mortem human brains on a clinical MRI scanner. *Neuroimage* 2011;57(1):167-181.
34. Augustinack JC, van der Kouwe AJ, Blackwell ML, Salat DH, Wiggins CJ, Frosch MP, Wiggins GC, Potthast A, Wald LL, Fischl BR. Detection of entorhinal layer II using 7Tesla [corrected] magnetic resonance imaging. *Ann Neurol* 2005;57(4):489-494.
35. Sengupta S, Fritz FJ, Harms RL, Hildebrand S, Tse DHY, Poser BA, Goebel R, Roebroeck A. High resolution anatomical and quantitative MRI of the entire human occipital lobe ex vivo at 9.4T. *Neuroimage* 2018;168:162-171.
36. Droby A, Lukas C, Schanzer A, Spiwoks-Becker I, Giorgio A, Gold R, De Stefano N, Kugel H, Deppe M, Wiendl H, Meuth SG, Acker T, Zipp F, Deichmann R. A human post-mortem brain model for the standardization of multi-centre MRI studies. *Neuroimage* 2015;110:11-21.
37. Wilhelm MJ, Ong HH, Wehrli SL, Li C, Tsai PH, Hackney DB, Wehrli FW. Direct magnetic resonance detection of myelin and prospects for quantitative imaging of myelin density. *Proc Natl Acad Sci U S A* 2012;109(24):9605-9610.
38. Sheth VR, Fan S, He Q, Ma Y, Annese J, Switzer R, Corey-Bloom J, Bydder GM, Du J. Inversion recovery ultrashort echo time magnetic resonance imaging: A method for simultaneous direct detection of myelin and high signal demonstration of iron deposition in the brain - A feasibility study. *Magn Reson Imaging* 2017;38:87-94.
39. Kanawaku Y, Someya S, Kobayashi T, Hirakawa K, Shiotani S, Fukunaga T, Ohno Y, Kawakami S, Kanetake J. High-resolution 3D-MRI of postmortem brain specimens fixed by formalin and gadoteridol. *Leg Med (Tokyo)* 2014;16(4):218-221.
40. Dietrich O, Raya JG, Reeder SB, Reiser MF, Schoenberg SO. Measurement of signal-to-noise ratios in MR images: influence of multichannel coils, parallel imaging, and reconstruction filters. *J Magn Reson Imaging* 2007;26(2):375-385.
41. Yushkevich PA, Piven J, Hazlett HC, Smith RG, Ho S, Gee JC, Gerig G. User-guided 3D active contour segmentation of anatomical structures: significantly improved efficiency and reliability. *Neuroimage* 2006;31(3):1116-1128.
42. Acosta-Cabronero J, Hall LD. Measurements by MRI of the settling and packing of solid particles from aqueous suspensions. *AIChE Journal* 2009;55(6):1426-1433.
43. Henkelman RM. Measurement of signal intensities in the presence of noise in MR images. *Med Phys* 1985;12(2):232-233.
44. Schofield MA, Zhu Y. Fast phase unwrapping algorithm for interferometric applications. *Opt Lett* 2003;28(14):1194-1196.
45. Li W, Wu B, Liu C. Quantitative susceptibility mapping of human brain reflects spatial variation in tissue composition. *Neuroimage* 2011;55(4):1645-1656.
46. Liu T, Wisnieff C, Lou M, Chen W, Spincemaille P, Wang Y. Nonlinear formulation of the magnetic field to source relationship for robust quantitative susceptibility mapping. *Magn Reson Med* 2013;69(2):467-476.
47. Alkemade A, de Hollander G, Keuken MC, Schafer A, Ott DVM, Schwarz J, Weise D, Kotz SA, Forstmann BU. Comparison of T2*-weighted and QSM contrasts in Parkinson's disease to visualize the STN with MRI. *PLoS One* 2017;12(4):e0176130.

48. Meguro R, Asano Y, Odagiri S, Li C, Iwatsuki H, Shoumura K. Nonheme-iron histochemistry for light and electron microscopy: a historical, theoretical and technical review. *Arch Histol Cytol* 2007;70(1):1-19.
49. Kilsdonk ID, Jonkman LE, Klaver R, van Veluw SJ, Zwanenburg JJ, Kuijter JP, Pouwels PJ, Twisk JW, Wattjes MP, Luijten PR, Barkhof F, Geurts JJ. Increased cortical grey matter lesion detection in multiple sclerosis with 7 T MRI: a post-mortem verification study. *Brain* 2016;139(Pt 5):1472-1481.
50. De Reuck J, Auger F, Cordonnier C, Deramecourt V, Durieux N, Pasquier F, Bordet R, Maurage CA, Leys D. Comparison of 7.0-T T(2)*-magnetic resonance imaging of cerebral bleeds in post-mortem brain sections of Alzheimer patients with their neuropathological correlates. *Cerebrovasc Dis* 2011;31(5):511-517.
51. Krebs N, Langkammer C, Goessler W, Ropele S, Fazekas F, Yen K, Scheurer E. Assessment of trace elements in human brain using inductively coupled plasma mass spectrometry. *J Trace Elem Med Biol* 2014;28(1):1-7.
52. Betts MJ, Acosta-Cabronero J, Cardenas-Blanco A, Nestor PJ, Duzel E. High-resolution characterisation of the aging brain using simultaneous quantitative susceptibility mapping (QSM) and R2* measurements at 7T. *Neuroimage* 2016;138:43-63.
53. Thelwall PE, Shepherd TM, Stanisz GJ, Blackband SJ. Effects of temperature and aldehyde fixation on tissue water diffusion properties, studied in an erythrocyte ghost tissue model. *Magn Reson Med* 2006;56(2):282-289.
54. Birkl C, Soellradl M, Toeglhofer AM, Krassnig S, Leoni M, Pirpamer L, Vorauer T, Krenn H, Haybaeck J, Fazekas F, Ropele S, Langkammer C. Effects of concentration and vendor specific composition of formalin on postmortem MRI of the human brain. *Magn Reson Med* 2018;79(2):1111-1115.
55. Evia AM, Kotrotsou A, Tamhane AA, Dawe RJ, Kapasi A, Leurgans SE, Schneider JA, Bennett DA, Arfanakis K. Ex-vivo quantitative susceptibility mapping of human brain hemispheres. *PLoS One* 2017;12(12):e0188395.
56. Flygare WH. Molecular Magnetic Moments and Susceptibility in Formaldehyde. *The Journal of Chemical Physics* 1965;42(5):1563-1568.
57. Peters AM, Brookes MJ, Hoogenraad FG, Gowland PA, Francis ST, Morris PG, Bowtell R. T2* measurements in human brain at 1.5, 3 and 7 T. *Magn Reson Imaging* 2007;25(6):748-753.
58. Porea A, Webb AG. Reversible and irreversible effects of chemical fixation on the NMR properties of single cells. *Magn Reson Med* 2006;56(4):927-931.
59. Schmierer K, Parkes HG, So PW, An SF, Brandner S, Ordidge RJ, Yousry TA, Miller DH. High field (9.4 Tesla) magnetic resonance imaging of cortical grey matter lesions in multiple sclerosis. *Brain* 2010;133(Pt 3):858-867.
60. McAleese KE, Firbank M, Hunter D, Sun L, Hall R, Neal JW, Mann DM, Esiri M, Jellinger KA, O'Brien JT, Attems J. Magnetic resonance imaging of fixed post mortem brains reliably reflects subcortical vascular pathology of frontal, parietal and occipital white matter. *Neuropathol Appl Neurobiol* 2013;39(5):485-497.

Supporting Information for online publication

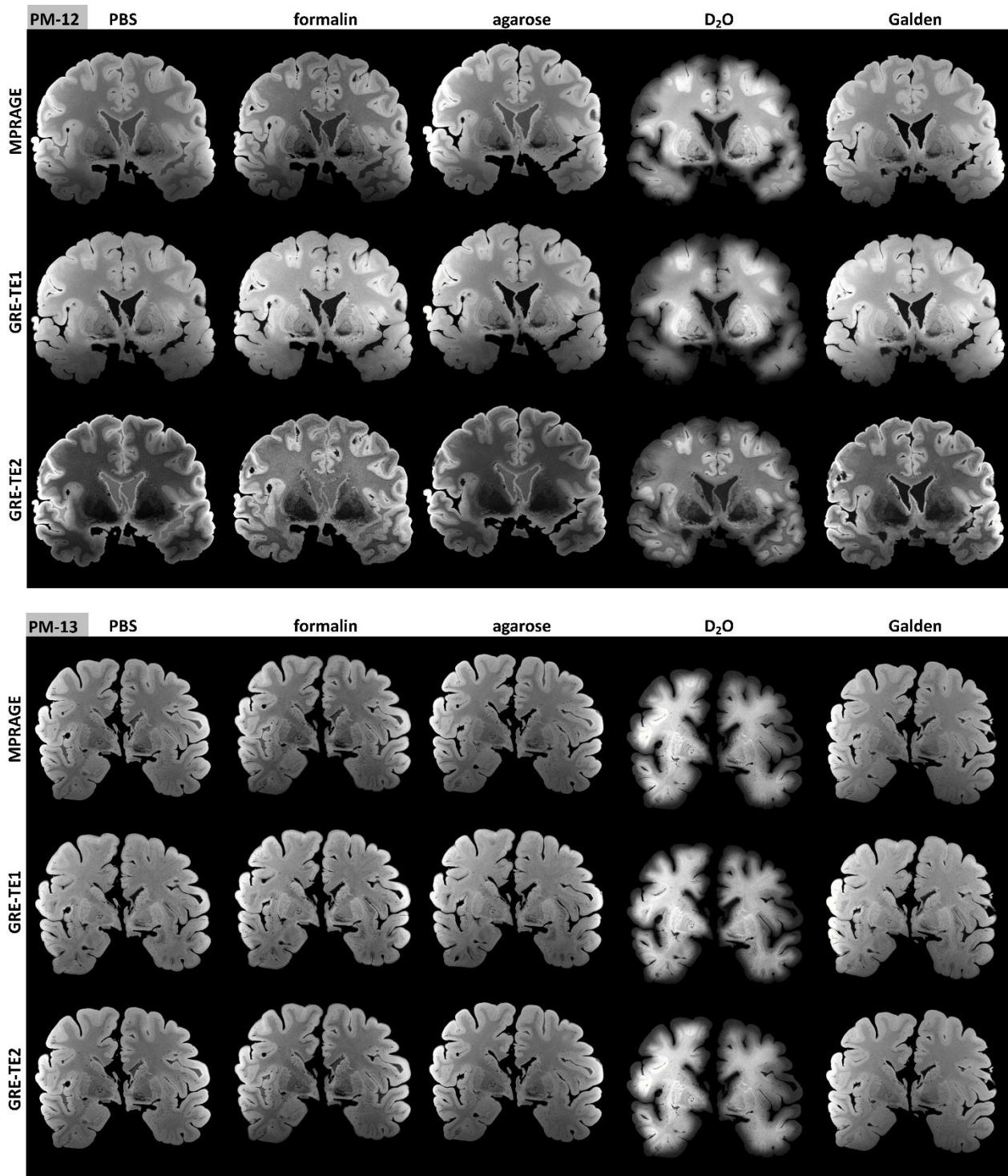
Supporting Information Figure S1. T₂* relaxation time evolution in different embedding media

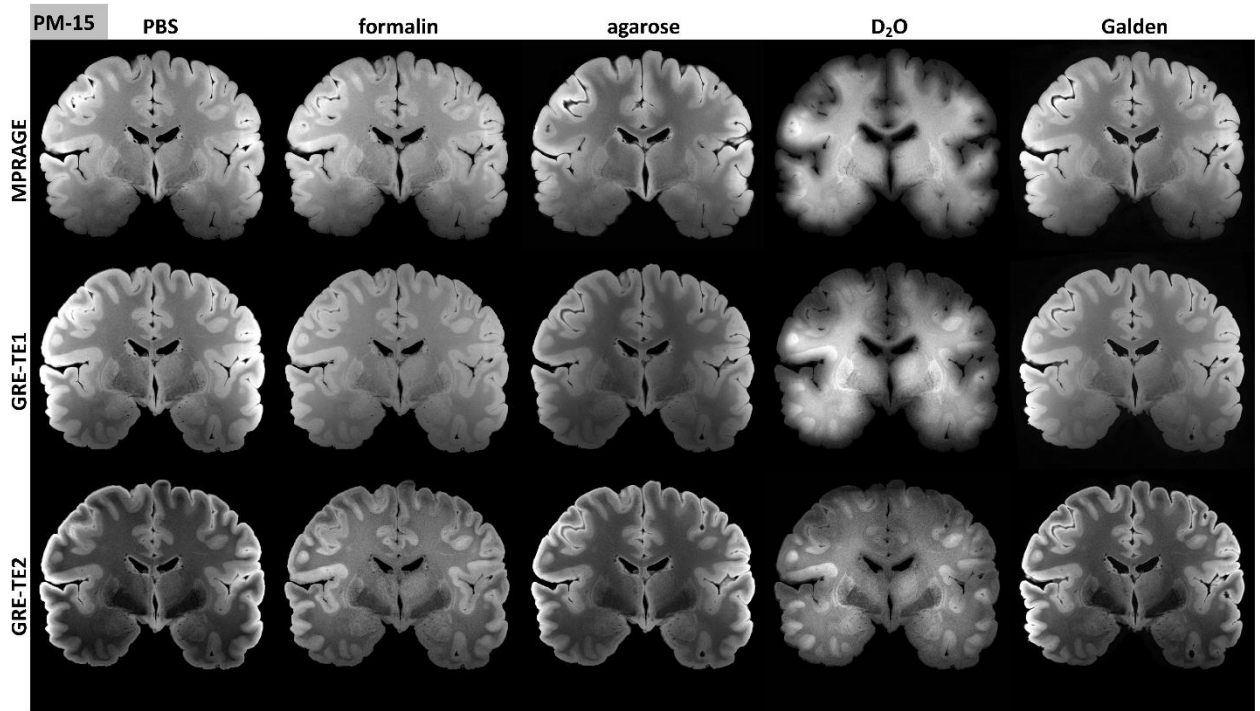
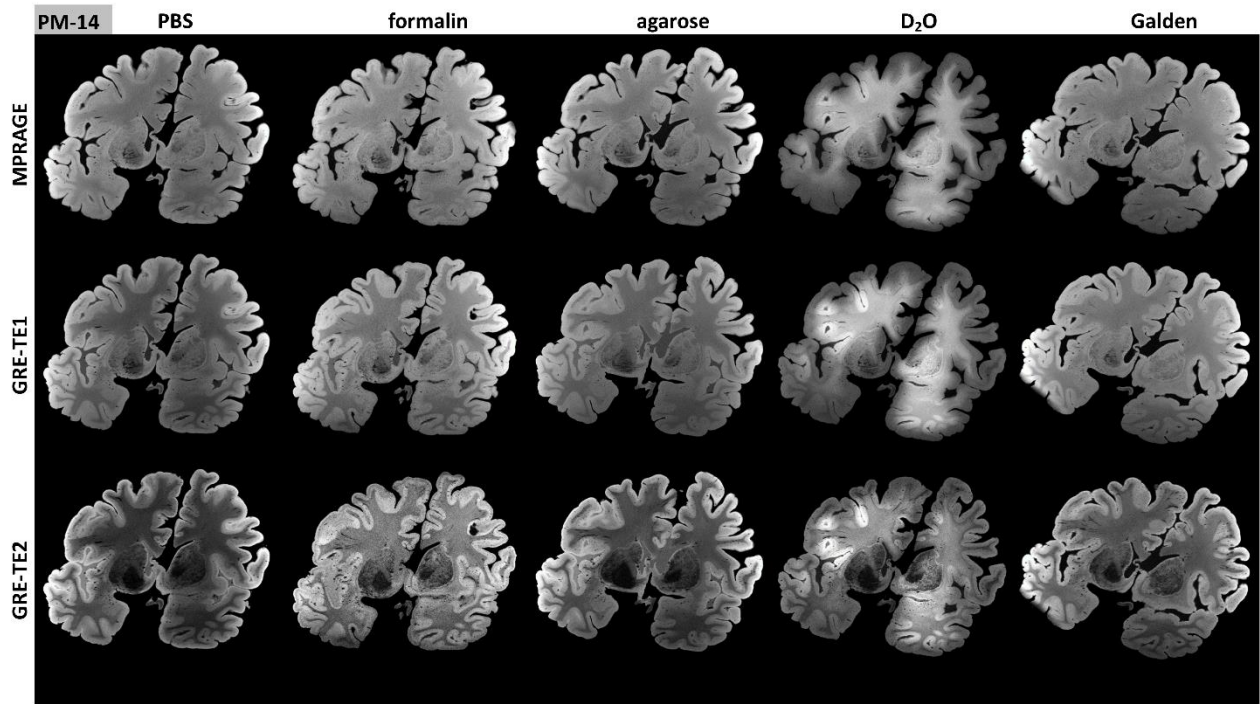
The evolution of mean (\pm SD) T₂* relaxation time (in milliseconds) in cortex (blue), white matter (red), and lentiform nucleus (green) in individual specimens after embedding in particular medium. Continuous scanning was stopped after a 'plateau' was reached. This required 5 to 23 hours for PBS and up to 5 hours for D₂O; there was no T₂* relaxation time evolution for Galden and agarose. Dashed arrows denote exchange of fresh PBS. The increase of T₂* relaxation time, most remarkably occurring in the cortex, is possibly a result of free-formalin having been washed out from the sample.

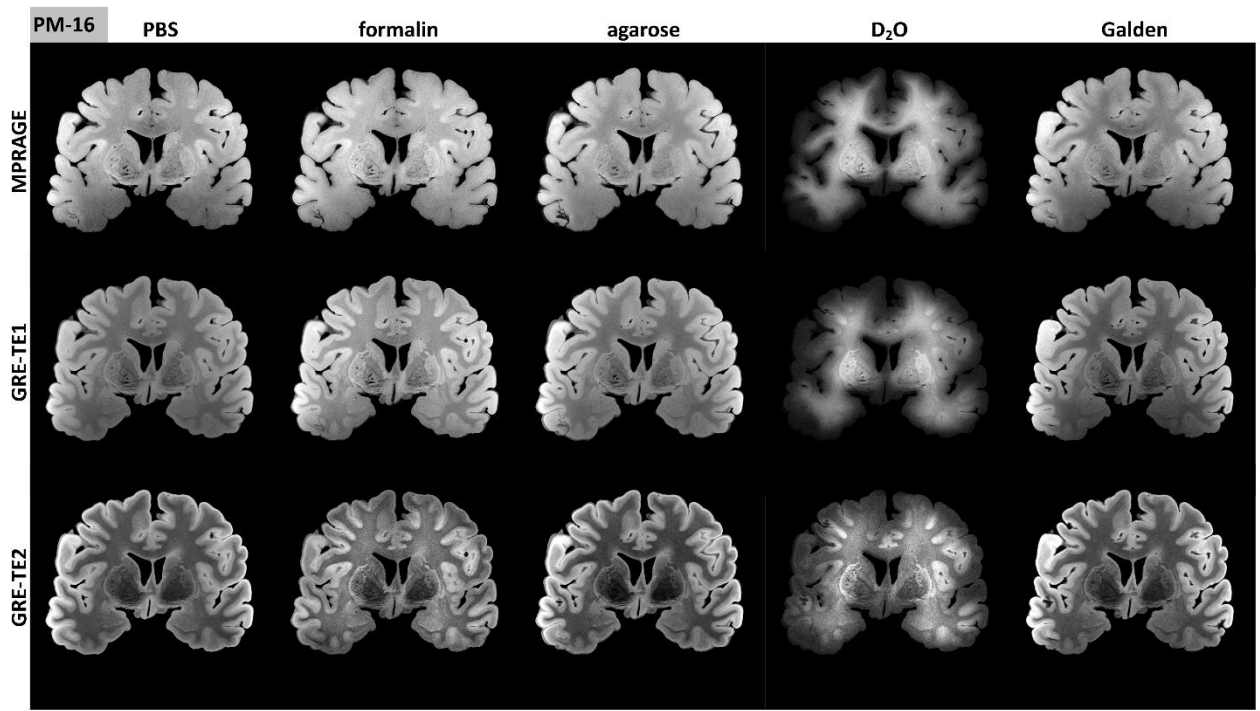


Supporting Information Figure S2. Comparison of MR images examined in different embedding media

MPRAGE, GRE-TE1, and GRE-TE2 high-resolution structural images of all samples (PM-12 – PM-16) examined in different embedding media. Display window width and window level are optimized individually for each image.

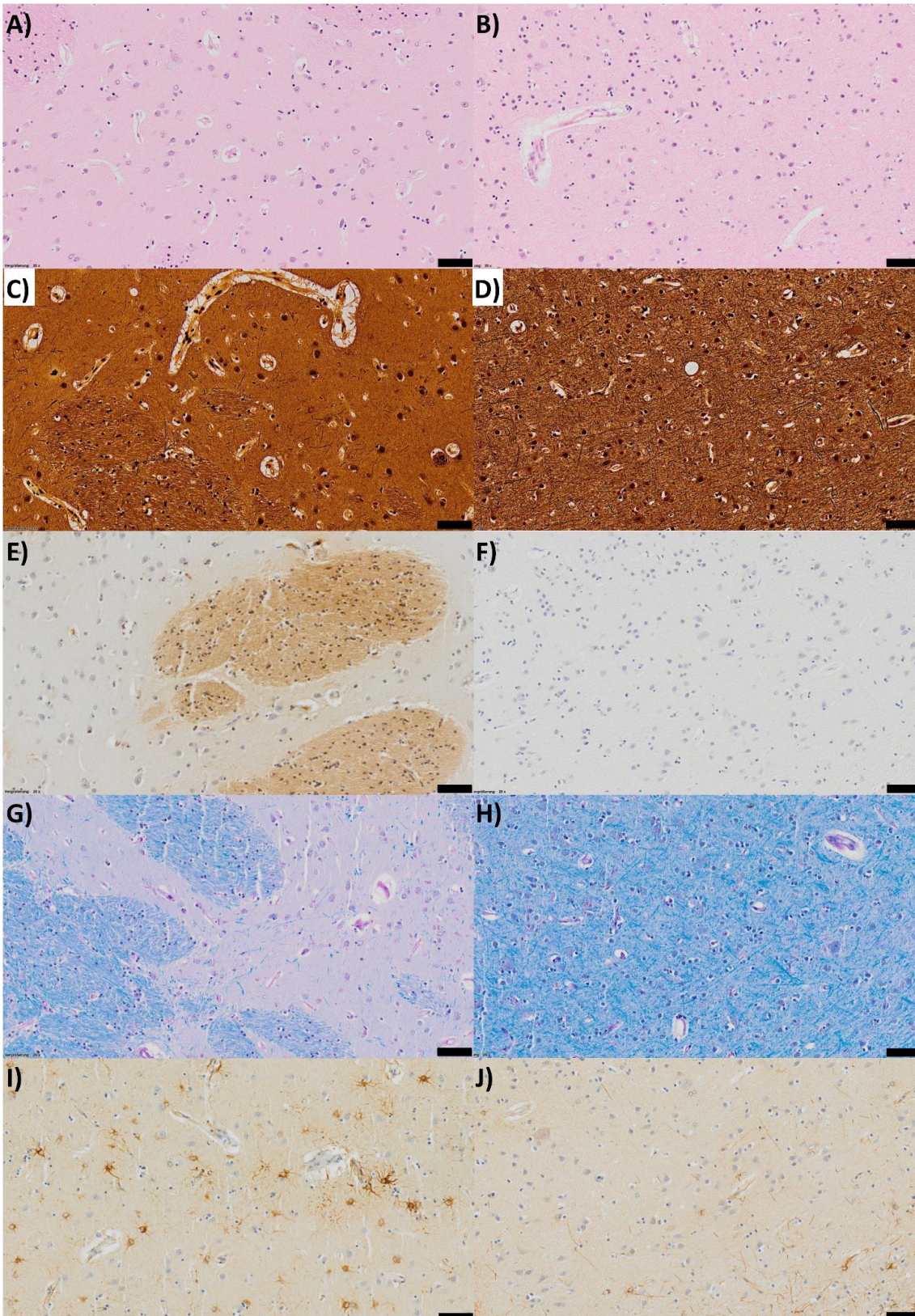






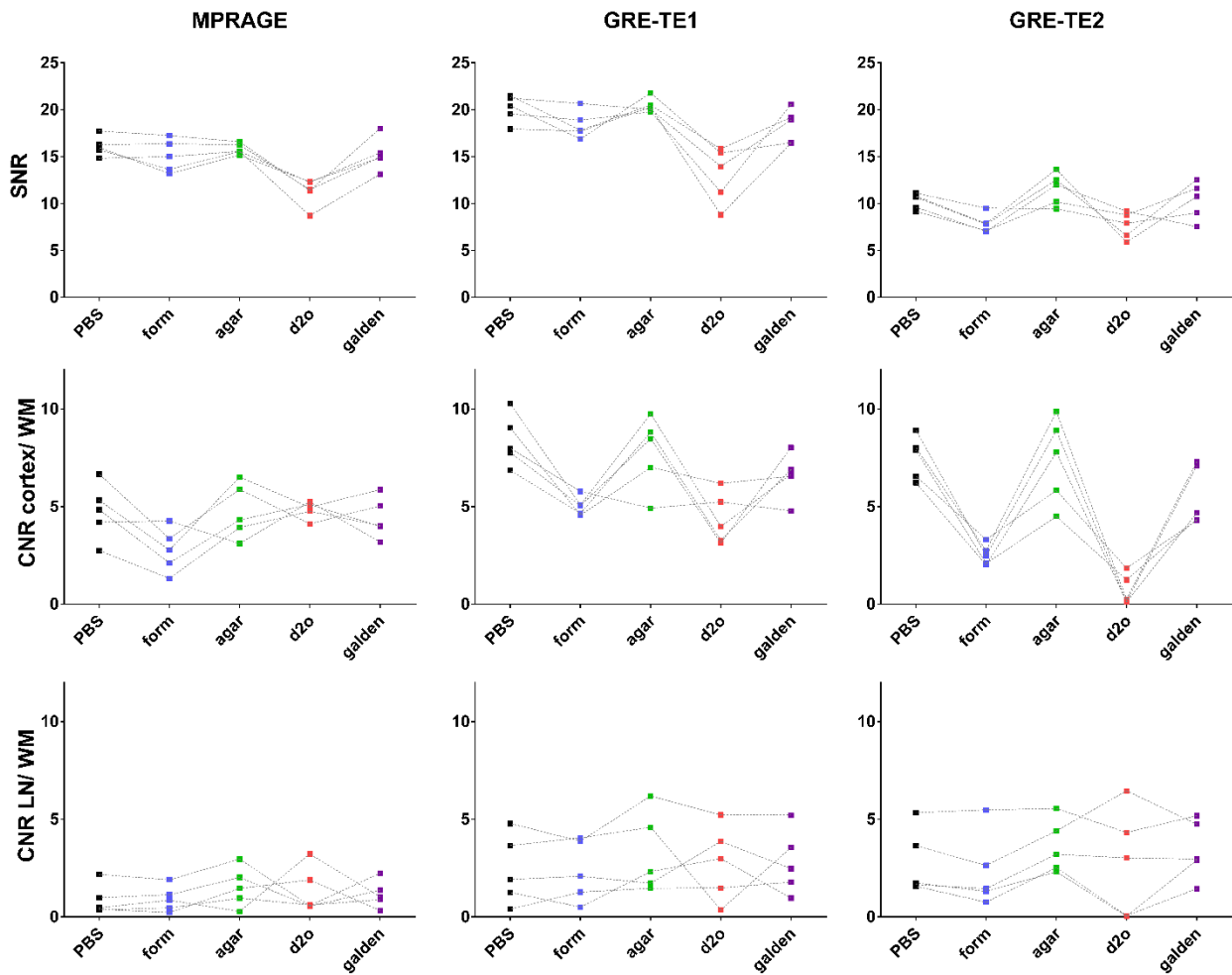
Supporting Information Figure S3. Neuropathological results

Staining of the lentiform nucleus and cortical region of the sample PM-14 are shown in the left and right column respectively. All employed methods, i.e. hematoxylin-eosin (A, B), Bielschowsky stain (C, D), DAB-enhanced Turnbull stain (E, F), luxol fast blue (G, H), and anti-gliial fibrillary acidic protein immunostaining (I, J), showed normal findings. Scale bars represent 50 μm .



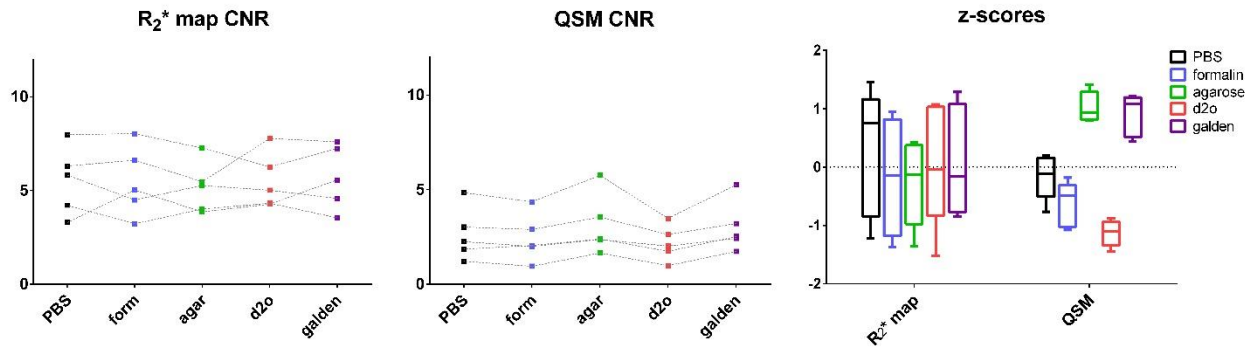
Supporting Information Figure S4. Signal-to-noise and contrast-to-noise ratio analysis

SNR (upper row), CNR between cortex and white matter (middle row) and between lentiform nucleus and white matter (bottom row) in MPRAGE, GRE-TE1, and GRE-TE2 images. Each specimens' SNRs and CNRs in different embedding media are shown by color dots connected with dashed line.



Supporting Information Figure S5. Contrast-to-noise ratio analysis in R_2^* and QSM quantitative maps

CNR of deep grey matter nuclei in R_2^* (left) and QSM (middle) quantitative maps. Each specimens' SNRs and CNRs in different embedding media are shown by color dots connected with dashed line. Z-scores of CNR values (right) calculated for each medium relative to the global behavior across all media for a given specimen and R_2^* and quantitative susceptibility maps.



Supporting Information Table S1. R_2^* values in different regions of interest and embedding media						
ROI	Sample	PBS	agarose	D2O	formalin	galden
GP	PMS12	0,145 (0,060)	0,142 (0,069)	0,134 (0,069)	0,164 (0,110)	0,131 (0,064)
	PMS13	0,121 (0,035)	0,116 (0,033)	0,118 (0,033)	0,122 (0,035)	0,116 (0,033)
	PMS14	0,150 (0,047)	0,138 (0,043)	0,140 (0,074)	0,170 (0,059)	0,141 (0,050)
	PMS15	0,113 (0,020)	0,104 (0,023)	0,109 (0,021)	0,120 (0,022)	0,098 (0,022)
	PMS16	0,108 (0,027)	0,094 (0,026)	0,103 (0,027)	0,113 (0,028)	0,095 (0,026)
Putamen	PMS12	0,103 (0,025)	0,097 (0,025)	0,091 (0,024)	0,114 (0,025)	0,089 (0,023)
	PMS13	0,092 (0,028)	0,089 (0,025)	0,089 (0,028)	0,094 (0,027)	0,088 (0,026)
	PMS14	0,094 (0,024)	0,081 (0,023)	0,078 (0,022)	0,105 (0,028)	0,082 (0,024)
	PMS15	0,073 (0,018)	0,064 (0,019)	0,069 (0,018)	0,080 (0,020)	0,061 (0,018)
	PMS16	0,068 (0,017)	0,055 (0,016)	0,062 (0,017)	0,074 (0,017)	0,057 (0,017)
CN	PMS12	0,078 (0,022)	0,072 (0,019)	0,071 (0,021)	0,106 (0,020)	0,070 (0,019)
	PMS13	0,074 (0,019)	0,072 (0,019)	0,071 (0,020)	0,077 (0,020)	0,072 (0,020)
	PMS14	0,071 (0,018)	0,063 (0,017)	0,059 (0,016)	0,094 (0,020)	0,066 (0,017)
	PMS15	0,043 (0,015)	0,035 (0,014)	0,037 (0,014)	0,072 (0,010)	0,037 (0,012)
	PMS16	0,059 (0,016)	0,046 (0,014)	0,050 (0,014)	0,076 (0,016)	0,047 (0,014)
WM	PMS12	0,061 (0,011)	0,055 (0,011)	0,048 (0,010)	0,081 (0,011)	0,051 (0,009)
	PMS13	0,045 (0,008)	0,044 (0,007)	0,044 (0,008)	0,046 (0,009)	0,044 (0,008)
	PMS14	0,063 (0,011)	0,049 (0,008)	0,047 (0,009)	0,075 (0,013)	0,052 (0,009)
	PMS15	0,064 (0,011)	0,050 (0,010)	0,058 (0,010)	0,076 (0,018)	0,048 (0,008)
	PMS16	0,062 (0,010)	0,047 (0,009)	0,052 (0,010)	0,069 (0,015)	0,049 (0,009)
Cortex	PMS12	0,034 (0,020)	0,031 (0,016)	0,026 (0,016)	0,067 (0,012)	0,029 (0,015)
	PMS13	0,035 (0,011)	0,033 (0,010)	0,030 (0,012)	0,045 (0,018)	0,036 (0,011)
	PMS14	0,037 (0,014)	0,030 (0,009)	0,027 (0,010)	0,071 (0,015)	0,035 (0,010)
	PMS15	0,047 (0,014)	0,032 (0,012)	0,036 (0,014)	0,069 (0,015)	0,032 (0,011)
	PMS16	0,037 (0,014)	0,026 (0,011)	0,028 (0,012)	0,060 (0,016)	0,028 (0,011)

Median R_2^* values in ms^{-1} and (interquartile ranges) are shown. Abbreviations: GP=globus pallidus; CN=caudate nucleus; WM=white matter

Supporting Information Table S2. Susceptibility values in different regions of interest and embedding media						
ROI	Sample	PBS	agarose	D2O	formalin	galden
GP	PMS12	0,041 (0,092)	0,040 (0,087)	0,050 (0,114)	0,057 (0,114)	0,046 (0,103)
	PMS13	0,041 (0,096)	0,016 (0,088)	0,040 (0,118)	0,044 (0,094)	0,036 (0,091)
	PMS14	0,035 (0,081)	0,017 (0,066)	0,023 (0,077)	0,042 (0,096)	0,031 (0,088)
	PMS15	0,016 (0,035)	0,027 (0,023)	0,028 (0,040)	0,017 (0,038)	0,016 (0,026)
	PMS16	0,015 (0,026)	0,021 (0,021)	0,024 (0,042)	0,011 (0,038)	0,012 (0,020)
Putamen	PMS12	0,031 (0,070)	0,020 (0,068)	0,035 (0,081)	0,038 (0,079)	0,034 (0,078)
	PMS13	0,030 (0,085)	0,009 (0,081)	0,031 (0,096)	0,040 (0,086)	0,033 (0,087)
	PMS14	0,019 (0,083)	0,013 (0,074)	0,021 (0,086)	0,005 (0,088)	0,019 (0,082)
	PMS15	0,014 (0,030)	0,023 (0,024)	0,025 (0,034)	0,009 (0,030)	0,016 (0,028)
	PMS16	0,007 (0,020)	0,009 (0,018)	0,015 (0,027)	0,004 (0,027)	0,002 (0,018)
CN	PMS12	0,021 (0,050)	0,019 (0,046)	0,030 (0,053)	0,036 (0,065)	0,037 (0,053)
	PMS13	0,017 (0,063)	0,000 (0,057)	0,027 (0,070)	0,025 (0,062)	0,025 (0,071)
	PMS14	0,014 (0,053)	0,003 (0,050)	0,008 (0,055)	0,009 (0,061)	0,009 (0,061)
	PMS15	0,000 (0,020)	0,010 (0,017)	0,010 (0,016)	-0,001 (0,021)	0,006 (0,015)
	PMS16	0,008 (0,020)	0,015 (0,018)	0,015 (0,019)	0,009 (0,024)	0,002 (0,020)
WM	PMS12	0,007 (0,030)	0,002 (0,029)	0,008 (0,029)	0,013 (0,035)	0,009 (0,031)
	PMS13	0,011 (0,043)	-0,010 (0,041)	0,008 (0,045)	0,014 (0,040)	0,010 (0,043)
	PMS14	0,007 (0,031)	-0,004 (0,027)	-0,002 (0,033)	0,000 (0,039)	-0,003 (0,033)
	PMS15	0,002 (0,013)	0,006 (0,010)	0,008 (0,016)	-0,004 (0,011)	0,003 (0,010)
	PMS16	0,005 (0,013)	0,005 (0,011)	0,008 (0,014)	-0,001 (0,012)	0,000 (0,010)
Cortex	PMS12	0,006 (0,014)	0,001 (0,014)	0,010 (0,011)	0,013 (0,018)	0,008 (0,019)
	PMS13	0,009 (0,027)	-0,013 (0,022)	0,009 (0,019)	0,015 (0,042)	0,010 (0,031)
	PMS14	0,004 (0,017)	-0,005 (0,011)	0,000 (0,012)	0,002 (0,029)	-0,004 (0,021)
	PMS15	0,000 (0,014)	0,005 (0,011)	0,009 (0,011)	-0,003 (0,013)	0,002 (0,012)
	PMS16	0,003 (0,012)	0,005 (0,009)	0,009 (0,008)	0,000 (0,014)	-0,002 (0,014)

Median susceptibility values in ppm and (interquartile ranges) are shown. Abbreviations: GP=globus pallidus; CN=caudate nucleus; WM=white matter

Supporting Information Table S3. Quantitative measurements in embedding media						
	formalin	PBS	D₂O	Galden	Agarose	Reference
R₂* (ms⁻¹)	0.049 ± 0.001	0.000 ± 0.000	n.a.	n.a.	0.010 ± 0.001	0.000 ± 0.000
QS (ppm)	-0.002 ± 0.000	-0.070 ± 0.000	n.a.	n.a.	-0.098 ± 0.003	0.000 ± 0.001

Reference is ultraclean water; vials are embedded in 1.5% agarose prepared from ultraclean water. QS values are referenced to the mean value from reference (1) and reference (2). Abbreviations: QS=quantitative susceptibility, n.a.= not available

Supporting Information Table S4. Comparison of embedding media				
	Approximate price per scan (200 ml; Euro)	Image quality	Advantages	Disadvantages
PBS	0.5	Overall good	cheap and readily available	none
Formalin	2	Low SNR in late echo images	no need for sample washing and waiting for equilibration between sample and embedding medium	increases R_2^* measurements trend for higher variance in susceptibility measurements
Agarose	10	Overall good	prevents sample motion	trend for higher variance in susceptibility measurements time consuming preparation of the agar
Galden	50 (can be reused)	Overall good	dark background	high-density fluid - difficult to submerge the specimen
D₂O	150	Low SNR	dark background	expensive, difficult to reuse